

Testing the consistency of three-point halo clustering in Fourier and configuration space

K. Hoffmann,^{1,2} ^{*} E. Gaztañaga², R. Scoccimarro³, M. Crocce²

¹Center for Astrophysics, Department of Physics, Tsinghua University, Beijing, 100084, China

²Institute of Space Sciences, IEEC-CSIC, Campus UAB, Carrer de Can Magrans, s/n, 08193 Barcelona, Spain

³Center for Cosmology and Particle Physics, Department of Physics, New York University, NY 10003, New York, USA

Accepted XXX. Received YYY; in original form ZZZ

ABSTRACT

We compare reduced three-point correlations Q of matter, haloes (as proxies for galaxies) and their cross correlations, measured in a total simulated volume of $\sim 100 (h^{-1}\text{Gpc})^3$, to predictions from leading order perturbation theory on a large range of scales in configuration space. Predictions for haloes are based on the non-local bias model, employing linear (b_1) and non-linear (c_2, g_2) bias parameters, which have been constrained previously from the bispectrum in Fourier space. We also study predictions from two other bias models, one local ($g_2 = 0$) and one in which c_2 and g_2 are determined by b_1 via an approximately universal relation. Overall, measurements and predictions agree when Q is derived for triangles with $(r_1 r_2 r_3)^{1/3} \gtrsim 60 h^{-1}\text{Mpc}$, where r_{1-3} are the sizes of the triangle legs. Predictions for Q_{matter} , based on the linear power spectrum, show significant deviations from the measurements at the BAO scale (given our small measurement errors), which strongly decrease when adding a damping term or using the non-linear power spectrum, as expected. Predictions for Q_{halo} agree best with measurements at large scales when considering non-local contributions. The universal bias model works well for haloes and might therefore be also useful for tightening constraints on b_1 from Q in galaxy surveys. Such constraints are independent of the amplitude of matter density fluctuation (σ_8) and hence break the degeneracy between b_1 and σ_8 , present in galaxy two-point correlations.

Key words: cosmology: large-scale structure of Universe - methods: statistical - numerical - analytical

1 INTRODUCTION

Higher-order correlations, induced by gravity into the distribution of large-scale matter density fluctuations, contain information which cannot be captured by second-order statistics. This information can be used to tighten constraints on cosmological models, as well as on models of galaxy formation. A key tool for obtaining such constraints are galaxy bias models (e.g. Desjacques et al. 2016). These models relate the density and the tidal field of the full matter content in a given region to the density of observable tracers, such as galaxies. They include a number of so-called bias parameters, which depend on the various processes that drive the tracer formation. Since these highly complex processes are only partly understood, the bias parameters cannot be predicted in a reliable way (e.g. Li et al. 2007; Müller et al. 2011; Pujol et al. 2017; Springel et al. 2017) and hence need to be measured from the data. Such measurements can be

obtained from the analysis of weak gravitational lensing signals, or redshift space distortions. However, these methods rely on good redshift estimations and imaging of the tracers (i.e. galaxies) as well as on various model assumptions. It is therefore interesting to obtain independent measurements of the bias parameters, which is possible with a joint analysis of second- and third-order statistics. This approach becomes increasingly interesting as errors on these statistics decrease with the increasing volumes of upcoming galaxy surveys. Going to third-order in the statistical analysis of galaxy surveys does not only deliver bias measurements, but also measurements of the growth of matter fluctuations. The latter provide the aforementioned cosmological constraints, while the bias can be used to predict the number of galaxies per halo, which places constraints on galaxy formation models (e.g. Scoccimarro et al. 2001; Berlind & Weinberg 2002; Cooray & Sheth 2002).

The most general third-order statistics is the three-point correlation function (hereafter referred to as 3PCF), which is defined in configurations space. Alternatively one

^{*} E-mail: hoffmann@tsinghua.edu.cn

can study its Fourier space counterpart, the bispectrum. These two statistics contain in principle the same information. However, their analyses implicate different limitations and challenges, which can affect the physical interpretation of the results. A main advantage of the bispectrum is that an analysis in Fourier space allows for a clear exclusion of high frequency modes in the density fluctuations, which are difficult to interpret theoretically due to their highly non-linear evolution. In configuration space, these high frequency modes contribute to the 3PCF in principle at all scales. In practice one therefore needs to restrict the analysis to large scales, where their contribution is negligible, lavishing a lot of valuable data. Another advantage of the bispectrum is that its covariance is diagonal for Gaussian density fluctuations. This approximation works well, even for evolved density fields, while deviations from Gaussianity can also be taken into account (Scoccimarro 2000; Sefusatti et al. 2006; Chan & Blot 2016). The covariance of the 3PCF on the other hand is not diagonal, even for Gaussian fluctuations, which makes the modeling more difficult (Srednicki 1993; Slepian & Eisenstein 2015). An additional difference in the analysis of the bispectrum and the 3PCF lies in the fact that the computation of the latter is more expensive. However, this aspect can be tackled by employing advanced algorithms and appropriate computational resources, as done in this work (see also, Barriga & Gaztañaga 2002; McBride et al. 2011a; Jarvis 2015; Slepian & Eisenstein 2015, and references therein). Besides its disadvantages, there are some arguments which speak for the 3PCF. One of them is the fact that the amplitude of the 3PCF (but not its errors) is not affected by shot-noise, whereas the latter affects the bispectrum amplitude at all scales and hence needs to be modelled for correcting the measurements. In addition, an analysis in configuration space has the advantage that complicated survey masks can be easily taken into account in the analysis of observational data, while in Fourier space such masks impose complicated effects on the measured bispectrum, which are difficult to model (e.g. Scoccimarro 2000). A more general consideration is that it is easier to interpret effects such as redshift space distortions or baryon acoustic oscillations (BAO) on the statistics in configuration space, since that is where the physical processes which cause these effects happen. Studies of third-order correlations in the literature usually focus on either Fourier or configuration space (e.g. McBride et al. 2011b; Marín et al. 2013; Gil-Marín et al. 2015). However, it is worthwhile studying both statistics and cross-check the results, since their different advantages and disadvantages are quite complementary.

In this work we will conduct such a cross-check for the first time. Our main interest thereby is to verify if and when the bias parameters, obtained from the bispectrum are consistent with those which affect the 3PCF in configuration space. Our approach is based on the analysis of Chan et al. (2012, hereafter referred to as CSS12). These authors measured the bias parameters of large-scale structure tracers in Fourier space from a set of N-body simulations, using a leading-order perturbative model of the bispectrum and restricting the analysis to large modes with wave numbers $k \leq 0.1 \text{ hMpc}^{-1}$. The tracers in their analysis are dark-matter halos, while the same method for measuring the bias can be applied to any other type of tracers, such as galaxies or galaxy clusters. For our cross-check we use the same per-

turbative model together with the bias parameters of CSS12 to predict the halo 3PCF in configuration space. We then measure the latter in the same set of simulations to test the predictions. This allows us to verify if and when the bias parameters measured from third-order statistics in Fourier space also describe the corresponding statistics in configuration space. Simultaneously we test at which scales, redshifts and halo mass ranges the leading order perturbative modeling of the 3PCF is an appropriate approximation.

1.1 Bias models tested

The bias model relates the density fluctuations and the tidal field of matter in a certain region to the density fluctuations of its tracers. These fluctuations are defined with respect to the mean density as $\delta \equiv (\rho - \bar{\rho})/\bar{\rho}$. Since the leading order perturbative expansion of third-order statistics, on which we focus in this analysis, is quadratic, we use the quadratic non-local bias model,

$$\delta_h = b_1 \left\{ \delta_m + \frac{1}{2} [c_2 (\delta_m^2 - \langle \delta_m^2 \rangle) + g_2 \mathcal{G}_2] \right\}. \quad (1)$$

The indices h and m refer to the halo and matter density fluctuations respectively. The parameters b_1 and c_2 are hereafter referred to as local linear and quadratic bias (Fry & Gaztanaga 1993), while g_2 will be referred to as quadratic non-local bias, since it scales with the tidal field term \mathcal{G}_2 , which can be generated by masses outside of the volume in which δ_g is defined (see CSS12; McDonald & Roy 2009; Baldauf et al. 2012). Note that the non-local bias has also been referred to as an additional local bias parameter, since the tidal field is a local observable, which depends on derivatives of the potential (see CSS12, Desjacques et al. 2016). However, in this work we call it non-local, since it is non-local in the density.

We use three sets of bias parametrizations for predicting the 3PCF. The *first set* consists of the bias parameters b_1 , $c_2 \equiv b_2/b_1$ and $g_2 \equiv 2\gamma_2/b_1$, obtained by CSS12 from fitting the non-local bias model predictions for the bispectrum at leading order to measurements in the same set of simulations as studied in this work. Here b_2 and γ_2 are the quadratic local and the non-local bias parameters respectively, in the notation of CSS12. The *second set* equals the first set, except for the non-local bias parameter g_2 , which is set to zero in order to verify the impact of the non-local contributions on the 3PCF predictions. In the *third set* the linear bias b_1 is the only input parameter. This is the same parameter, as in the two previous sets, but was obtained by CSS12 from fits of the linear bias model ($\delta_h = b_1 \delta_m$) to the power spectrum. The quadratic local bias parameter c_2 in this third set is computed from the (approximately) universal relation $c_2 \simeq 0.77b_1^{-1} - 2.43 + b_1$, given by Hoffmann et al. (2017) (see also Hoffmann et al. 2015b; Lazeyras et al. 2016, for similar relations). The non-local bias in the third set is obtained from the local Lagrangian model, $g_2 = -(4/7)(1 - 1/b_1)$. The three sets of bias model parameters are summarised in Table 1 and will in the following be referred to as *non-local*, *local* and *$b_{\delta^2 f_{ix}}$* model respectively.

For a three-dimensional analysis of real spectroscopic surveys one would further need to take into account redshift space distortions in the modeling. Redshift space distortions cancel out approximately at large scales

Table 1. Different bias models studied in this work. The bias parameters have been measured in Fourier space from the same set of simulations by CSS12. For the $b_{\delta^2 fix}$ model we use a roughly universal relation for the quadratic local bias $c_2(b_1)$ (Hoffmann et al. 2017) and the local Lagrangian model for the quadratic non-local $g_2(b_1)$.

bias model	description
non-local	b_1, c_2, g_2 from bispectrum fits
local	same b_1 and c_2 as above, $g_2 = 0$
$b_{\delta^2 fix}$	b_1 from power spectrum fits, $c_2 = 0.77b_1^{-1} - 2.43 + b_1$, $g_2 = -(4/7)(1 - 1/b_1)$

in the reduced 3PCF (defined in Section 2.1, see e.g. Gaztañaga & Scoccimarro 2005), but there are non-linear contributions that could be as large as the non-local terms. There is some indication in simulations that non-local terms can cancel out with redshift space distortions, (e.g. Fig.17 in Hoffmann et al. 2015a), but this requires further study. Large volume photometric surveys, such as DES or LSST will provide additional constraints from weak lensing of the projected 3PCF, both of galaxy and matter correlations, as well as galaxy-matter cross-correlations. Since those surveys measure redshifts from broad-band photometry these probes will have little contamination by redshift space distortions. All this is beyond the scope of this paper, but should be a clear continuation of our study.

2 THREE-POINT CORRELATIONS Q

2.1 Definitions

Our 3PCF analysis is applied on density fields $\rho^x(\mathbf{r})$, where x refers to the density of matter ($x = m$) or of its tracers, such as galaxies or, as in our case, dark matter halos ($x = h$) at the position \mathbf{r} . The density fields are smoothed with a top-hat filter of scale R and described by the normalised density fluctuations $\delta^x(\mathbf{r}_i) \equiv \delta_i^x$, introduced in Section 1.1. Note that, in contrast to the notation in equation (1), we now set x as upper index to avoid confusion between the position and the power indices in the following. The 3PCF can be defined as the average product of density fluctuations at three positions $(\mathbf{r}_1, \mathbf{r}_2, \mathbf{r}_3)$, which form a triangle. In the case of the halo-matter-matter cross-correlations it is written as

$$\zeta^{hmm}(r_{12}, r_{13}, r_{23}) \equiv \langle \delta_1^h \delta_2^m \delta_3^m \rangle(r_{12}, r_{13}, r_{23}), \quad (2)$$

where $r_{ij} \equiv |\mathbf{r}_i - \mathbf{r}_j|$ are the absolute values of the triangle legs and $\langle \dots \rangle$ denotes the average over all possible triangle orientations and translations. We proceed by defining the symmetric reduced three-point cross-correlation,

$$Q_\times \equiv \frac{1}{3} \frac{\zeta^{hmm} + \zeta^{hmm} + \zeta^{mmh}}{\zeta_H^\times} \quad (3)$$

and drop the expression *reduced* in the following. The hierarchical three-point cross-correlation in the denominator, defined as

$$\zeta_H^\times \equiv \xi_{12}^{hm} \xi_{13}^{hm} + \xi_{12}^{mh} \xi_{23}^{hm} + \xi_{13}^{mh} \xi_{23}^{mh}, \quad (4)$$

is comprised of two-point cross-correlations $\xi_{ij}^{xy} \equiv \langle \delta_i^x \delta_j^y \rangle(r_{ij})$ between the density fields x and y (e.g.

Peebles & Groth 1975; Fry 1984). The corresponding expressions for the three-point auto correlations for matter and halos, (Q_m and Q_h respectively) are defined analogously, i.e. $Q_m \equiv \zeta^{mmm}/\zeta_H^{mmm}$ and $Q_h \equiv \zeta^{hhh}/\zeta_H^{hhh}$.

2.2 Modeling

Our predictions for Q_h and Q_\times are based on the non-local quadratic bias model from equation (1), which yields at leading-order perturbative expansion in terms of δ_m

$$Q_h \simeq \frac{1}{b_1} [Q_m + c_2 + g_2 Q_{nloc}], \quad (5)$$

where b_1 and c_2 are the local linear and quadratic bias parameters respectively. The non-local contribution Q_{nloc} scales with the non-local quadratic bias parameter g_2 (see CSS12; Baldauf et al. 2012). The corresponding leading order expression for the halo-matter-matter cross-correlation is given by

$$Q_\times \simeq \frac{1}{b_1} [Q_m + \frac{1}{3}(c_2 + g_2 Q_{nloc})]. \quad (6)$$

Equation (5) has an important application in the analysis of galaxy surveys, since it allows for bias measurements which are independent of the linear growth of matter fluctuations (e.g. Frieman & Gaztanaga 1994; Sefusatti et al. 2006; McBride et al. 2011b; Marín et al. 2013; Gil-Marín et al. 2015) and hence breaks the growth-bias degeneracy. However, cosmological constraints from such bias measurements are limited by the inaccuracies of the Q_h modeling as explained in the following.

The statistics of the full matter field, Q_m and Q_{nloc} , cannot be observed in galaxy surveys and hence need to be predicted for a given cosmology. Q_m is therefore often predicted from N-body simulations. This approach has also been used by CSS12 for measuring the bias parameters in their simulations, as it captures the non-linear contributions to Q_m . However, these authors employ an analytical expression for the quadratic non-local contribution Q_{nloc} , which is in Fourier space simply related to the cosine of the angle between two wave vectors. Direct measurements of Q_{nloc} would be more complicated (see Section 3.2). Another disadvantage of deriving the Q_m and Q_{nloc} from simulations, is that a dense sampling of the cosmological parameter space for deriving constraints from observations would require enormous resources (albeit Q_m and Q_{nloc} are independent of the linear growth factor and hence only weakly depend on cosmology at large scales). In this analysis we will therefore employ predictions from leading order perturbation theory for Q_m and Q_{nloc} (Jing & Boerner 1997; Gaztanaga & Bernardreau 1998; Barriga & Gaztañaga 2002; Bel et al. 2015). These leading order approximations, as well as those of Q_h and Q_\times in equation (5) and (6) introduce inaccuracies in the modeling, in particular at small triangle scales, which are strongly affected by high frequency, non-linear modes (Scoccimarro et al. 1998; Pollack et al. 2012).

Measurements of the different 3PCFs in N-body simulations allow us to validate these approximations. For comparing Q_h and Q_\times with such measurements, we employ bias parameters measured from the power spectrum and the bispectrum in Fourier space by CSS12 in the same set of simulations as used in this analysis. We thereby do not

only test the validity of the perturbation theory predictions for the 3PCFs, but also if the bias parameters in Fourier and configuration space are consistent with each-other. Note that the Fourier space bias measurements are also based on leading order perturbation theory predictions for the cross-bispectrum B_{hmm} and the non-local contribution. However, non-linear contributions can be excluded in that case in a more reliable way than in configuration space by restricting the analysis to long wavelength modes. We therefore consider them to be robust.

To summarise, the accuracy of the model of Q_h in equation (5) depends on the accuracy of the leading order perturbative expansion of Q_h , Q_m and Q_{nloc} . The comparison with measurements in simulations will further depend on the accuracy of the bias measurements in Fourier space. In Section 3 we will test these different model ingredients using measurements of Q_m , Q_h and Q_\times .

2.3 Measurements in simulations

We verify the model predictions using the same set of $N_{sim} = 49$ cosmological N-body simulations, which was analysed by CSS12. Each simulation was run with 640^3 dark matter particles, which reside in a cube with comoving side length of $1280 h^{-1}\text{Mpc}$, which results in a total simulated volume of $\sim 100 (h^{-1}\text{Gpc})^3$. The cosmological parameters were set to $\Omega_m = 1 - \Omega_\Lambda = 0.27$, with $\Omega_b = 0.046$, $h = 0.72$, $n_s = 1$ and $\sigma_8 = 0.9$. Halos were identified as *friends-of-friends* groups with a linking length of 0.2 of the mean particle separation. We split them into the same mass samples as CSS12, which are summarised in Table 2.

For measuring the 3PCFs in these simulations we generate density maps of the simulated halo and matter distributions based on $8 h^{-1}\text{Mpc}$ cubical cells. The products of density contrasts $\delta_1\delta_2\delta_3$, over which we average to compute Q , are obtained from triplets of these cells, which we find using an algorithm described by Barriga & Gaztañaga (2002). This algorithm delivers measurements for triangle configurations, defined by the fixed leg sizes r_1, r_2 at different opening angles $\alpha \equiv \arccos(\hat{\mathbf{r}}_1 \cdot \hat{\mathbf{r}}_2)$. The fixed triangle legs are defined with a tolerance $r_i \pm \delta r$, while we set δr to values between 1 and $4 h^{-1}\text{Mpc}$, depending on the triangle configuration. This tolerance is needed for finding a large number of triplets on the grid and thereby reduce the impact of shot-noise on the 3PCF measurements. We tested for the configurations $(r_1, r_2) = (48, 24)$, $(64, 32)$ and $(80, 48) h^{-1}\text{Mpc}$ that uncertainties coming from this tolerance are small compared to inaccuracies of the 3PCF models studied in this paper. The 3PCFs are computed for 28 configurations (r_1, r_2) , with 18 opening angles each, which leads to a total number of 504 triangles.

2.4 Error estimation

To quantify the deviations between the mean 3PCF measurements from the 49 simulations, \bar{Q}_i , and the corresponding model predictions, Q_i^{mod} , for a set of N_∇ triangles (each defined by r_1, r_2 and α , with $i \in \{1, 2, \dots, N_\nabla\}$), we want

Table 2. Halo mass samples with corresponding linear bias from the halo-matter cross-power spectrum from CSS12. The same samples are used in this work.

z	halo sample	mass range [$10^{13} M_\odot/h$]	b_{hm}^P
0.0	m0	4 – 7	1.43
0.0	m1	7 – 15	1.75
0.0	m2	> 15	2.66
0.5	m0	3 – 5	1.88
0.5	m1	5 – 10	2.26
0.5	m2	> 10	3.29
1.0	m0	2 – 3.1	2.43
1.0	m1	3.1 – 5.7	2.86
1.0	m2	> 5.7	3.99

to compute

$$\chi^2 = \sum_{ij}^{N_\nabla} \Delta_i \hat{C}_{ij}^{-1} \Delta_j, \quad (7)$$

where $\Delta_i \equiv (Q_i^{mod} - \bar{Q}_i)/\sigma_i$. The standard deviation of \bar{Q}_i is given by $\sigma_i^2 = \langle (Q_i - \bar{Q}_i)^2 \rangle / N_{sim}$, while $\langle \dots \rangle$ denotes the mean over the N_{sim} measurements. The factor $1/N_{sim}$ accounts for the fact that we study the deviations of the mean measurements from the prediction, rather than deviations of measurements in individual realisations. The normalised covariance (or correlation) matrix is hence given by

$$\hat{C}_{ij} = \langle \Delta_i \Delta_j \rangle / N_{sim}, \quad (8)$$

with $\Delta_i \equiv (Q_i - \bar{Q}_i)/\sigma_i$. We choose $N_\nabla < N_{sim}$ to allow for the inversion of C_{ij} , as pointed out by Hartlap et al. (2007), and set $N_\nabla = 30$ for the χ^2 measurements shown in this paper. We tested that these measurements are consistent, but noisier (less noisy) when setting $N_\nabla = 20$ (40), which presumably results from the relatively low number of 49 realisations. To reduce this noise, we follow Gaztañaga & Scoccimarro (2005) by performing a Singular Value Decomposition of the covariance (hereafter referred to as SVD), i.e.

$$\hat{C}_{ij} = (U_{ik})^\dagger D_{kl} V_{lj}. \quad (9)$$

The diagonal matrix $D_{kl} = \delta_{kl} \lambda_k^2$ consists of the singular values λ_j (SVs), while the corresponding normalised modes $\hat{\mathbf{M}}_i$ form the matrix U . The modes associated to the largest SVs may be understood analogously to eigenvectors. We tested that they build a nearly orthogonal basis, in which we can approximate equation (7) as

$$\chi^2 \simeq \sum_i^{N_{mode}} \langle \Delta_i \hat{\mathbf{M}}_i \rangle^2 / \lambda_i^2. \quad (10)$$

Note that here $\langle \dots \rangle$ denotes the scalar product, i.e. the projection of Δ_i on $\hat{\mathbf{M}}_i$, while Δ_i is the same quantity which appears in equation (7). Fig. B2 shows that \hat{C}_{ij} is typically dominated only by a few modes. Assuming that the modes with the lowest SVs can be associated with measurement noise, we use only SVs with values larger than the sampling error estimate (i.e. $\lambda^2 \gtrsim \sqrt{2/N_{sim}}$) for our χ^2 computation, as suggested by Gaztañaga & Scoccimarro (2005). The number of selected modes is hence the degree of freedom in our χ^2 estimation, i.e. d.o.f. = $N_{mode} < N_{bin} < N_{sim}$.

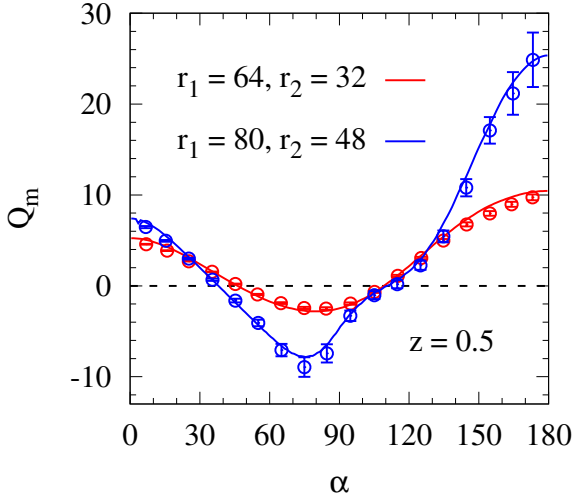


Figure 1. Reduced matter 3PCF Q_m for triangles with fixed legs r_1 and r_2 (size is indicated in $h^{-1}\text{Mpc}$) versus the mean triangle opening angle $\alpha \equiv \arccos(\hat{\mathbf{r}}_1 \cdot \hat{\mathbf{r}}_2)$ in each bin. Symbols show mean measurements from 49 simulations with 1σ errors at redshift $z = 0.5$. Lines show tree-level predictions from the measured (non-linear) power spectrum.

3 ACCURACY OF Q PREDICTIONS

The accuracy of bias measurements from the reduced three-point halo auto-correlation Q_h in observations depends on how well it is approximated by the leading order perturbative model, given by equation (5). To verify this model we test its different components separately with direct measurements in the simulations described in Section 2.3. We start with testing the modeling of Q_m in Section 3.1 and proceed in Section 3.2 with tests of the quadratic component in equation (5). Our measurements of the latter are obtained by combining the three-point auto- and cross-correlations, Q_h and Q_\times respectively. Finally, we compare the complete predictions for Q_h and Q_\times , given by equation (5) and (6), with the measurements in the simulations in Section 3.3. For modeling the quadratic components we use bias parameters measured by CSS12 in the same set of simulations, using a leading order perturbative approximation of the 3PCF in Fourier space, i.e. the tree-level bispectrum. In addition we employ simple relations between the linear and the quadratic bias parameters, i.e. $b_2(b_1)$ and $g_2(b_1)$. This leaves b_1 as the only free input parameter in the bias model, which we adopt from the fits to the power spectrum, given by CSS12 (see Section 1.1).

3.1 Q_m

We start our verification of the Q_m model from leading order (tree level) perturbation theory (hereafter referred to as Q_m^{PT} , see Section 2.2) by comparing its predictions to measurements in simulations. As examples we show in Fig. 1 results at redshift $z = 0.5$ for triangles with fixed legs $(r_1, r_2) = (64, 32)$ and $(80, 48) h^{-1}\text{Mpc}$ versus the triangle opening angle $\alpha \equiv \arccos(\hat{\mathbf{r}}_1 \cdot \hat{\mathbf{r}}_2)$. The Q_m measurements are the mean results of the 49 simulations and are shown with 1σ errors bars. Here and throughout the paper we display meas-

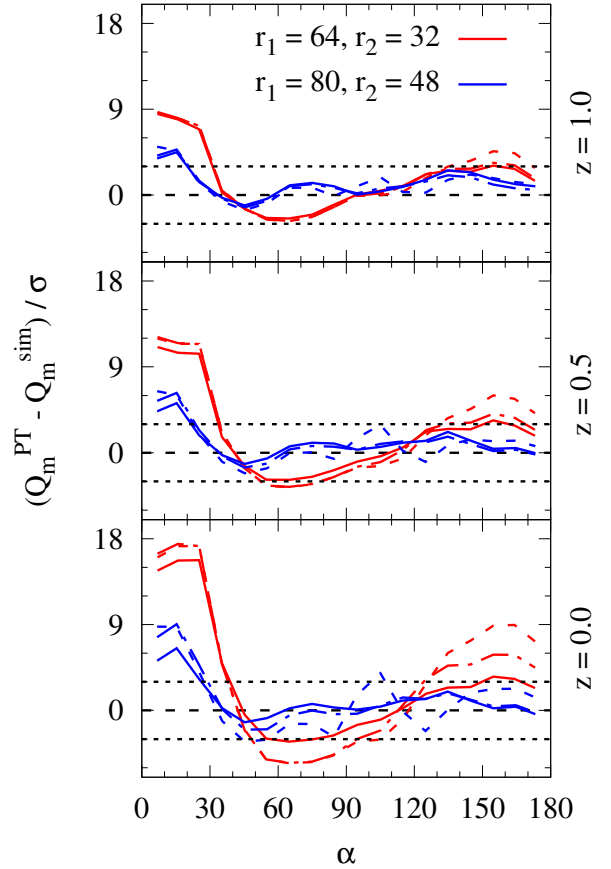


Figure 2. Significance of the deviations between the mean reduced matter 3PCF, measured in 49 simulations and different tree-level predictions for the same triangle configurations as shown in Fig. 1. Dashed and solid lines show predictions from the linear and the measured (non-linear) power spectrum respectively. Predictions based on the de-wiggled power spectrum are shown as dashed-dotted lines. The black dotted lines mark 3σ deviations from the measurements.

urements at the mean opening angle in each bin. The predictions in Fig. 1 are computed from the non-linear power spectrum, which was measured in the simulations. Both, measurements and predictions exhibit a u-shape, which is more strongly pronounced for the larger triangle configuration and originates from the filamentary structure of the cosmic web. The measurements clearly show the baryonic acoustic oscillations (BAO) feature for the $(80, 48) h^{-1}\text{Mpc}$ configuration at around 100° (see e.g. Gaztañaga et al. 2009; Slepian et al. 2017, who found hints of similar 3PCF features in real data). This BAO feature is well described by the predictions.

The significance of the deviations between measurements and predictions is shown for all redshifts in Fig. 2. In addition to the predictions from the non-linear power spectrum, we show in this figure also results based on the linear as well as the so-called de-wiggled power spectrum (hereafter also referred to as P_{lin} and P_{dw} respectively). The latter introduces non-linearities around the BAO scale in the 3PCF, coming from large-scale displacements (Crocce & Scoccimarro 2008; Carlson et al. 2013; Baldauf et al. 2015; Senatore & Zaldarriaga 2015; Blas et al. 2016). It consists of the no-wiggle approximation

of the power spectrum (P_{nw}) from Eisenstein & Hu (1998), P_{lin} and a smearing function, i.e., $P_{dw} \equiv P_{nw} + (P_{lin} - P_{nw})\exp(-k^2\sigma_v)$, where k is the wave number and σ_v is the variance of the displacement field (Eisenstein et al. 2007)¹.

As a general trend we see in Fig. 2 that all predictions differ more significantly from the measurements for smaller triangles. This can be explained by the interplay of two effects. On one hand, terms in the perturbative expansion of Q_m beyond leading order, which are neglected in our Q_m model, contribute stronger at smaller scales. This explanation is consistent with the fact that the deviations are less significant at higher redshift and also when Q_m^{PT} is computed from the non-linear, instead of the linear power spectrum. On the other hand, the signal-to-noise ratio is higher at small scales (see bottom panel of Fig. A2). Note that the latter is specific to the joint volume of our 49 realisations of roughly $\sim 100 (h^{-1}\text{Gpc})^3$. For the smaller volumes of current and near future galaxy surveys we expect the model to deviate less significantly because of larger measurement errors.

Predictions from the de-wiggled power spectrum are very similar to those from the linear power spectrum for smaller triangles (e.g. $(r_1, r_2) = (64, 32) h^{-1}\text{Mpc}$, $\alpha \lesssim 120^\circ$) and agree well with those from the non-linear power spectrum for large triangles (i.e. $(r_1, r_2) = (80, 48) h^{-1}\text{Mpc}$, $\alpha \gtrsim 90^\circ$). The latter finding indicates that for the tree-level calculation of the 3PCF in configurations space, implementing resummations over large-scale displacements by using the de-wiggled power spectrum has almost the same effect as using the non-linear spectrum from the simulation. For both cases the predictions are in 1σ agreement with the measurements at the BAO scale, while using the linear spectrum leads to $2 - 3\sigma$ deviations. For the remainder of our analysis we will use predictions based on the non-linear power spectrum, as they show the best overall agreement with the measurements in Fig. 2.

A convenient way to show results for all triangles in our analysis is to display them for a given opening angle α versus the triangle size, here defined as $\sqrt{r_1 r_2}$. As an example we show the measurements of Q_m in Fig. 3. This figure demonstrates the strong increase of the u-shape of $Q_m(\alpha)$ with the triangle scale. The minimum lies between 60 and 90° . Measurements for $\alpha \gtrsim 120^\circ$ and $\sqrt{r_1 r_2} \gtrsim 50$ are dominated by noise.

The significance of the deviations between Q_m model predictions and measurements are shown for redshift $z = 0.5$ versus α and $\sqrt{r_1 r_2}$ in Fig. 4. We find that Q_m^{PT} is below the measurements for opening angles between roughly $30 - 90^\circ$ for triangles with $30 \lesssim \sqrt{r_1 r_2} \lesssim 50 h^{-1}\text{Mpc}$. For smaller and larger opening angles the predictions tend to lie above the measurements. Similar results based on simulations with different cosmologies have been reported in the literature (see for instance Barriga & Gaztañaga (2002) or Hoffmann et al. (2015a), who use the same algorithms for the Q_m predictions and measurements as employed in

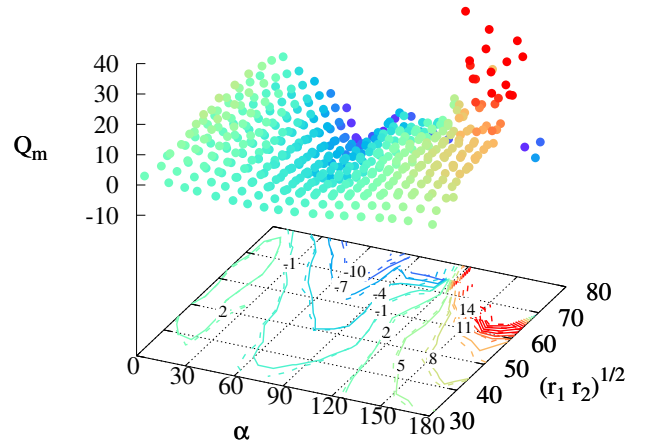


Figure 3. Q_m measurements at $z = 0.5$ versus the mean triangle opening angle per bin α and triangle scale $(r_1 r_2)^{1/2}$. Dots and solid contour lines show mean results from 49 simulations. Dashed contour lines show tree-level predictions based on the non-linear power spectrum. The colours indicate the amplitude of Q_m .

this study). Scoccimarro et al. (1998) showed that such deviations can be explained by higher order contributions as they reduce when the predictions are developed to next to leading order, including 1-loop terms (see also Sefusatti et al. 2010). As in Fig. 2 one can see in the top panel of Fig. 4 that using the linear power spectrum leads to strong deviations between predictions and measurements, in particular around the BAO peak, which are apparent as a red banana-shaped feature. This BAO feature follows roughly triangles with $r_3 \sim 95 h^{-1}\text{Mpc}$, which are marked in the top panel as black lines. The deviations strongly reduce when the predictions are computed from the non-linear power spectrum for triangles scales $\sqrt{r_1 r_2} \gtrsim 50 h^{-1}\text{Mpc}$ and $\alpha \gtrsim 30$ to roughly 1σ .

Defining the overall triangle size as $(r_1 r_2 r_3)^{1/3}$, we find that the deviations converge to 2σ at $(r_1 r_2 r_3)^{1/3} \gtrsim 60 (80) h^{-1}\text{Mpc}$, when using the non-linear (linear) power spectrum (Fig. A2). Triangles with $(r_1 r_2 r_3)^{1/3} = 60 h^{-1}\text{Mpc}$ are therefore marked by black lines in the bottom panel of Fig. 4). The normalised Q_m covariance matrix, shown in Fig. B1, reveals that the Q_m measurements for different triangles are correlated with each other. Hence, we compute an SVD estimate of the χ^2 in bins of $(r_1 r_2 r_3)^{1/3}$ to quantify the deviation between measurements and predictions, taking the covariance into account, as described in Section 2.4. Each $(r_1 r_2 r_3)^{1/3}$ bin includes measurements from 30 triangles, while we tested that our results change only weakly, when using 20 and 40 triangles per bin and do not affect our conclusions.

In Fig. 5, we find $\chi^2/d.o.f.$ values between 10 and 100 for $(r_1 r_2 r_3)^{1/3} \lesssim 50 h^{-1}\text{Mpc}$ at $z = 1.0$, where the degree of freedom ($d.o.f.$) is the number of singular values used for the χ^2 estimation. At $z = 0.0$ the $\chi^2/d.o.f.$ values are higher at small scales, indicating that Q_m predictions agree better with measurements at higher redshifts. At $(r_1 r_2 r_3)^{1/3} \gtrsim 60 h^{-1}\text{Mpc}$ the $\chi^2/d.o.f.$ values are roughly constant, taking values between $0.6 - 4$. An exception are the high values for

¹ We find that replacing the velocity dispersion with the quantity $\Sigma^2(r_{BAO}) \equiv \int_0^\Lambda P(k) d^3k / (3k^2) [1 - j_0(kr_{BAO}) + 2j_2(kr_{BAO})]$ (with j_n being the spherical Bessel function of order n , Baldauf et al. 2015), has a negligibly small effect on the de-wiggled predictions, compared to the deviations from other predictions or the measurements.

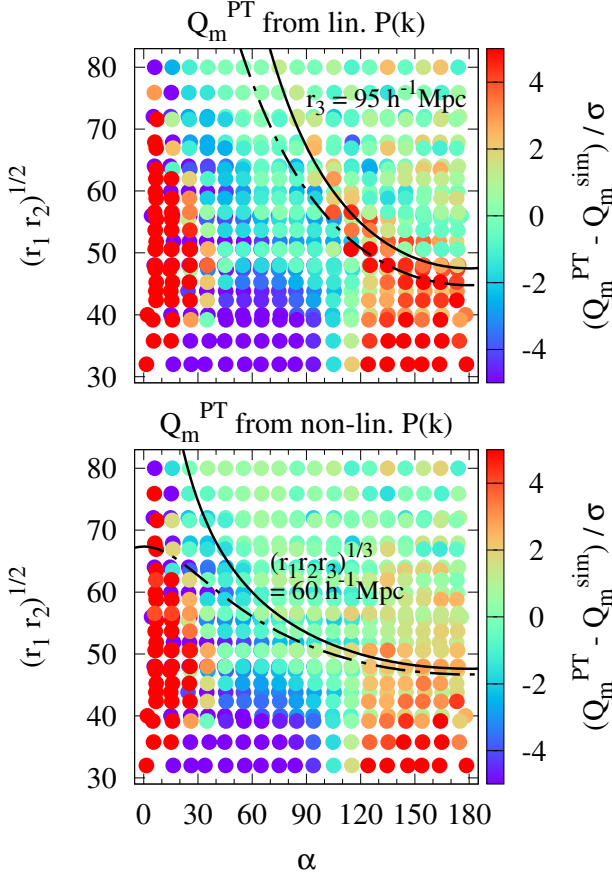


Figure 4. Significance of the deviations between Q_m measurements and tree-level predictions versus the mean triangle opening angle per bin α and the triangle scale $(r_1 r_2)^{1/2}$ in $h^{-1}\text{Mpc}$ at redshift $z = 0.5$. The predictions are derived from the linear and measured (non-linear) power spectrum (top and bottom panel respectively). Black lines in the top panel trace the BAO feature $(r_1 r_2)^{1/2}(\alpha)$ for $r_3 = 95 h^{-1}\text{Mpc}$. In the bottom panel black lines indicate the triangle scale at which the model fails at 2σ , $(r_1 r_2 r_3)^{1/3} \simeq 60 h^{-1}\text{Mpc}$. In both cases solid and dashed-dotted lines correspond to triangle configurations with $r_2/r_1 = 1.0$ and 0.5 respectively.

the Q_m model from the linear power spectrum at $z = 0.0$, whereas using the non-linear and linear power spectra lead to similar results at $z = 1.0$. These results indicated that non-linear contributions have a significant effect in Q_m at small scales and low redshift and can partly be taken into account in the Q_m predictions by using the non-linear power spectrum.

Note that the differences between results at different redshifts do not only result from different model performance, but also from differences in the covariances and modes selected for the χ^2 computation. Since these quantities are sensitive to noise we will not enter a detailed discussion.

3.2 ΔQ

In this subsection we test how well the higher-order contributions to the halo 3PCF are described by the quadratic $c_2 + g_2 Q_{nloc}$ term, which appears in equation (5) and (6). Fol-

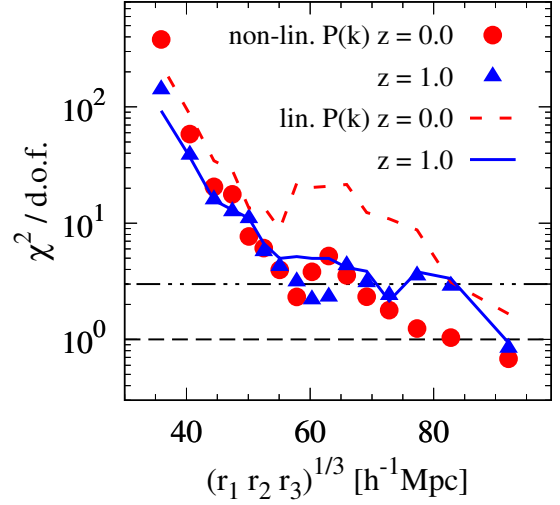


Figure 5. $\chi^2/\text{d.o.f.}$, quantifying the significance of the deviation between mean Q_m , measured in the simulations and tree-level predictions versus the mean triangle size $(r_1 r_2 r_3)^{1/3}$ per bin. Lines and symbols show results for Q_m predictions derived from the linear and non-linear power spectrum respectively at the redshifts $z = 0.0$ and $z = 0.5$.

lowing Bel et al. (2015), we obtain these higher-order contributions from the measurements by subtracting the halo-matter cross-correlation from the halo auto-correlation,

$$\Delta Q \equiv Q_h - Q_\times. \quad (11)$$

This subtraction leads to a cancellation of the linear Q_m/b_1 term in Q_h and Q_\times and hence isolates the higher-order terms. The aforementioned quadratic term correspond to the leading order perturbative approximation of ΔQ , which follows from inserting the corresponding leading order approximations for Q_h and Q_\times from equation (5) and (6) into equation (11), i.e.

$$\Delta Q \simeq \frac{2}{3b_1}(c_2 + g_2 Q_{nloc}). \quad (12)$$

The relation above allows us to test on one hand the accuracy of the quadratic model for the higher order terms in Q_h and Q_\times , independently of inaccuracies in the Q_m modeling, which we studied previously in Section 3.1. On the other hand, we test simultaneously if the bias parameters, which we adopt from the Fourier space measurements of CSS12, also describe the clustering statistics in configurations space. Regarding the latter case we employ three sets of bias parameters to which we refer to as local, non-local and $b_{\delta^2 fix}$ bias model, as described in Table 1, Section 1.1.

The corresponding model predictions for ΔQ are compared to the measurements at different triangle opening angles in Fig. 6. For this comparison we use the halo sample m2 at redshift $z = 0.5$ (defined in Table 2) and the same triangle configurations as for the Q_m in Fig. 1. The ΔQ measurements in Fig. 6 show a clear dependence on the triangle opening angle α for the small $(r_1, r_2) = (64, 32) h^{-1}\text{Mpc}$ triangle configuration. This finding contrasts the local bias model prediction of a constant $\Delta Q = 2c_2/3b_1$. However, at intermediate angles ($60^\circ \lesssim \alpha \lesssim 120^\circ$) the local model

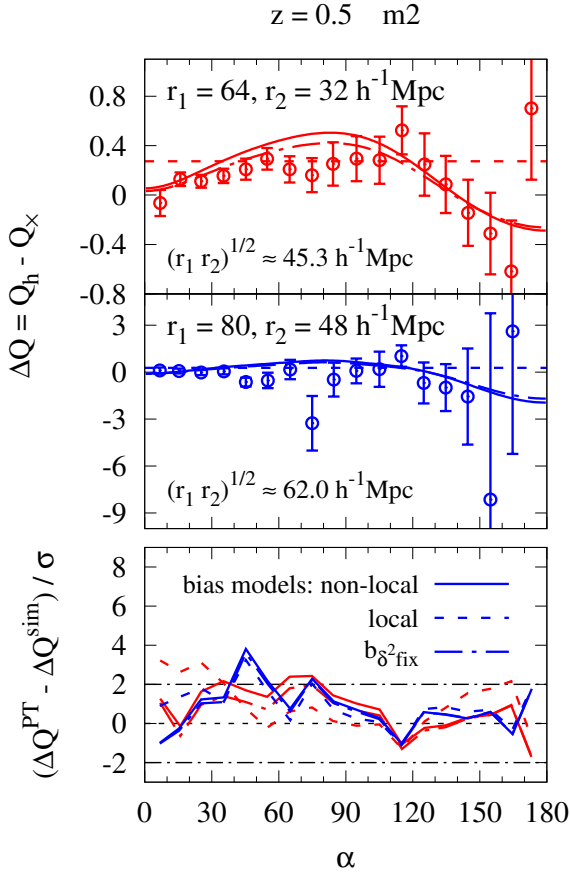


Figure 6. Top panels: ΔQ versus the mean triangle opening angle per bin $\alpha \equiv \arccos(\hat{\mathbf{r}}_1 \cdot \hat{\mathbf{r}}_2)$, measured at $z = 0.5$ for the mass sample m2. Dashed and solid lines show tree-level predictions from the local and non-local bias model respectively, using the non-linear power spectrum and bias parameters measured in Fourier space by CSS12 in equation (12). Bottom panel: the significance of the deviation between model predictions and measurements.

predictions are in better agreement with the measurements than predictions from the non-local model. This result indicates that neglected higher order terms might compensate the quadratic non-local contribution.

Similar trends are apparent for the larger $(80, 48) \text{ h}^{-1} \text{ Mpc}$ triangle configuration, while here the large measurement errors lead to a similar significance of the different model deviations (see bottom panel of Fig. 6).

Note that for the presented results we computed Q_{nloc} in equation (12) from the non-linear power spectrum, which was measured in the simulation. This is motivated by the fact that the Q_m model performs better in that case (see Section 3.1). However, using Q_{nloc} predictions from the linear power spectrum delivers very similar result and does not affect the conclusions drawn above.

Extending the comparison between models and measurements to all triangles in our analysis, we show in Fig. 7 the significance of the deviations between ΔQ measurements and model predictions versus the triangle opening angle and scale $\sqrt{r_1 r_2}$ (analogously to Fig. 4). We use again the mass sample m2 at $z = 0.5$ (with $b_1 = 3.29$) and show in addition also results for the sample m0 at $z = 0.0$ (with $b_1 = 1.43$) to

explore how differences in the bias effect the model performance. For the highly biased sample m2 at $z = 0.5$ (bottom panel of Fig. 7) the results line up with those for the two single triangle configurations, shown Fig. 6. For small triangles with $\sqrt{r_1 r_2} \lesssim 40 \text{ h}^{-1} \text{ Mpc}$ and triangle opening angles in the range of $60^\circ - 120^\circ$ the local bias model is in better agreement with the measurements than the non-local model. Overall both models tend to overpredict the measurements at small triangle scales. The results for the $b_{\delta^2 \text{fix}}$ model are very similar to those from the non-local model. This is also the case when the latter is based on the $b_2(b_1)$ relation from Lazeyras et al. (2016).

These findings differ from those of the low biased sample m0 at $z = 0.0$ (shown in top panel of Fig. 7) in three aspects. The first aspect is that the local and non-local model tend to underpredict the measurements for $\sqrt{r_1 r_2} \lesssim 40 \text{ h}^{-1} \text{ Mpc}$. The second aspect is that for the low biased sample the local and non-local model perform equally well. This can be expected, since the non-local bias, measured by CSS12 is close to zero in that case. The third aspect is that the $b_{\delta^2 \text{fix}}$ model differs from non-local model. In fact, it agrees better with the measurements than the other models. One interpretation of this result could be that the $c_2(b_1)$ and $g_2(b_1)$ relation is more accurate than the Fourier space measurements of the bias parameters from CSS12. Alternatively one might conclude that inaccuracies of the $b_{\delta^2 \text{fix}}$ model compensate the neglected higher-order terms in the ΔQ model in equation (12), leading to a good agreement with the measurements by accident. To clarify this point one could repeat the exercise, using a model for ΔQ which is developed beyond second order. For a possible application of the $c_2(b_1)$ and $g_2(b_1)$ relations of the $b_{\delta^2 \text{fix}}$ model in observations it would be interesting to test the dependence of our results on the cosmological parameters used. For bias measurements in observations it is also interesting to note that deviations between measurements in our $\sim 100 (h^{-1} \text{ Gpc})^3$ volume and model predictions become insignificant for $\sqrt{r_1 r_2} \gtrsim 40 \text{ h}^{-1} \text{ Mpc}$ as the measurement errors increase with scale.

As for Q_m we find an overall convergence of the deviation between measurements and predictions for triangles with $(r_1 r_2 r_3)^{1/3} \gtrsim 60 \text{ h}^{-1} \text{ Mpc}$ in Fig. A3, which are marked in Fig. 7 with black lines. We quantify these deviations again by computing the χ^2 via SVD, taking into account the covariance between measurements at different scales in $(r_1 r_2 r_3)^{1/3}$ bins with 30 triangles. Note that the ΔQ covariance is typically dominated by shot noise, coming from the Q_h contribution, which can be seen in Fig. B1. The results, shown in Fig. 8 are in line with our finding from Fig. A3 as results converge to $\chi^2/d.o.f$ values around unity. The highly biased sample shows larger overall deviations between measurements and predictions, in particular for the non-local model at $(r_1 r_2 r_3)^{1/3} \lesssim 60 \text{ h}^{-1} \text{ Mpc}$. Results for the $b_{\delta^2 \text{fix}}$ model are similar to those from the non-local model at large scales, while at small scales the former performs better as its $\chi^2/d.o.f.$ values are lower.

3.3 Q_h and Q_x

After validating the linear and quadratic components for the Q_h and Q_x models separately in Section 3.1 and 3.2 we now compare the full models, given by equation (5) and (6) with the measurements in our simulations. As for ΔQ we focus on

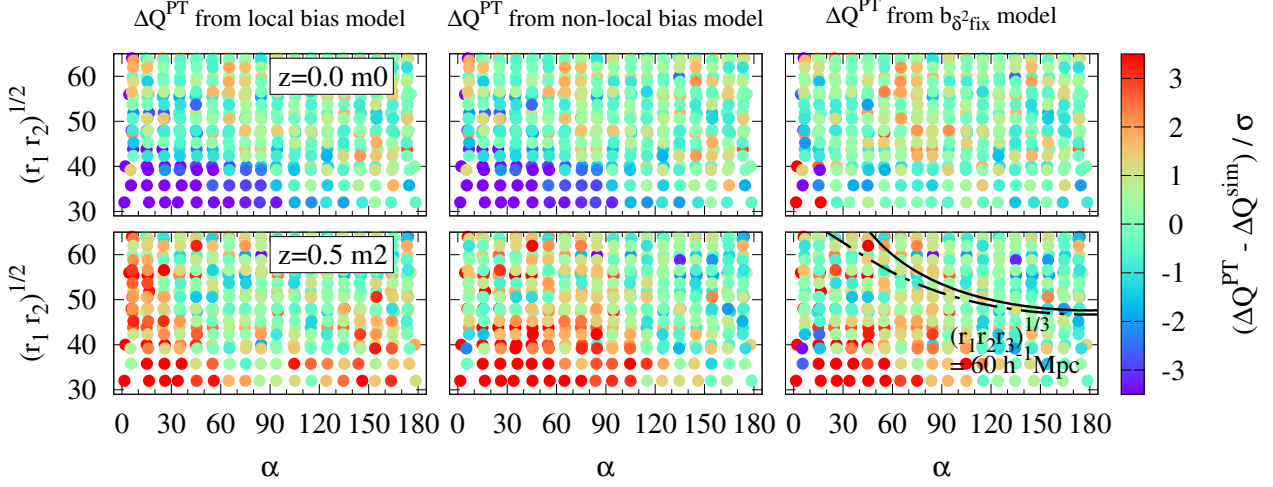


Figure 7. Significance of the deviations between predictions for ΔQ and measurements for the mass samples m0 at $z = 0.0$ and m2 at $z = 0.5$ (top and bottom panels respectively). The results are shown versus the mean triangle opening angles per bin α and triangle scales $(r_1 r_2)^{1/2}$ in $h^{-1}\text{Mpc}$. The predictions are derived from the local, the non-local and the $b_{\delta^2_{fix}}$ bias model (see Table 1), with bias parameters measured in Fourier space by CSS12. Solid and dashed black lines in the bottom right panel show $(r_1 r_2)^{1/2}(\alpha)$ for $(r_1 r_2 r_3)^{1/3} = 60 h^{-1}\text{Mpc}$ and triangle configurations of $r_1/r_2 = 0.5$ and 1.0 respectively.

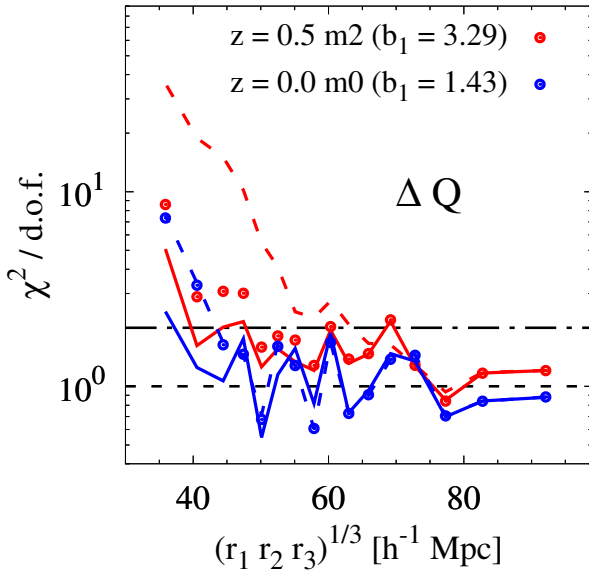


Figure 8. $\chi^2/\text{d.o.f.}$, quantifying the significance of the deviation between the mean ΔQ , measured in the simulations and predictions based on Fourier space bias parameters. Results are shown versus the mean triangle size $(r_1 r_2 r_3)^{1/3}$ per bin. Dots are results based on the predictions from the non-local bias model. Results from the local and the $b_{\delta^2_{fix}}$ bias model (see Table 1) are shown as dashed and solid lines respectively. Note that for the low biased mass sample m0 at redshift $z = 0.0$ the results for the local and non-local bias are very similar since the non-local bias contribution is very small.

model predictions, which are based on the non-linear power spectrum and start the analysis by showing Q_h and Q_\times , measured in the halo sample m2 at $z = 0.5$, for triangles with fixed legs of $(r_1, r_2) = (64, 32)$ and $(80, 48) h^{-1}\text{Mpc}$ versus the triangle opening angle α in Fig. 9. We find that the

models for both, Q_h and Q_\times tend to overpredict the measurements, which lines up with our corresponding results for ΔQ in Fig. 6. An exception of this trend are Q_h results from the small triangle configuration with $60 \lesssim \alpha \lesssim 90$. This indicates that the neglected terms in the perturbative model beyond leading order affect Q_h and Q_\times differently. Again, the model predictions based on the local bias model show the strongest deviations from the measurements, in particular for collapsed and relaxed triangles. This explains why neglecting the non-local term leads to an overestimation of the bias, when fitting Q_h or Q_\times model predictions to measurements (see CSS12). For such a fit one would choose a higher b_1 , since this would flatten the curve and deliver the measured shape. The overall amplitude can then be adjusted by varying c_2 (see equation (5)). Such fits of the local model are in fact in very good agreement with the measurements. However, the linear bias is too high (e.g. Manera & Gaztañaga 2011; Bel et al. 2015). Note that the linear bias measurements based on the local bias model would be too low instead of too high when using the 3PCF or the bispectrum, as explained by CSS12.

The best agreement between the Q_h and Q_\times measurements and the corresponding models occurs at large opening angles (hence large triangles) when using the non-local bias model ($1 - 2\sigma$). This scale dependence can be expected since errors increase and higher order contributions decrease with the scale. Results based on the $b_{\delta^2_{fix}}$ model are again very similar to those from the non-local model.

Interestingly the deviations between the model predictions and measurements are less significant for Q_h than for Q_\times , despite the fact that the neglected terms beyond leading order should have a higher contribution to Q_h and therefore lead to stronger deviations from the model. However, the errors on Q_h are more strongly affected by shot-noise than those for Q_\times ($\sigma_{Q_h}^2 \sim n_h^3$, $\sigma_{Q_\times}^2 \sim n_h$, where n_h is the halo number density). This means that for observations with similar or larger errors than our measurements, a development

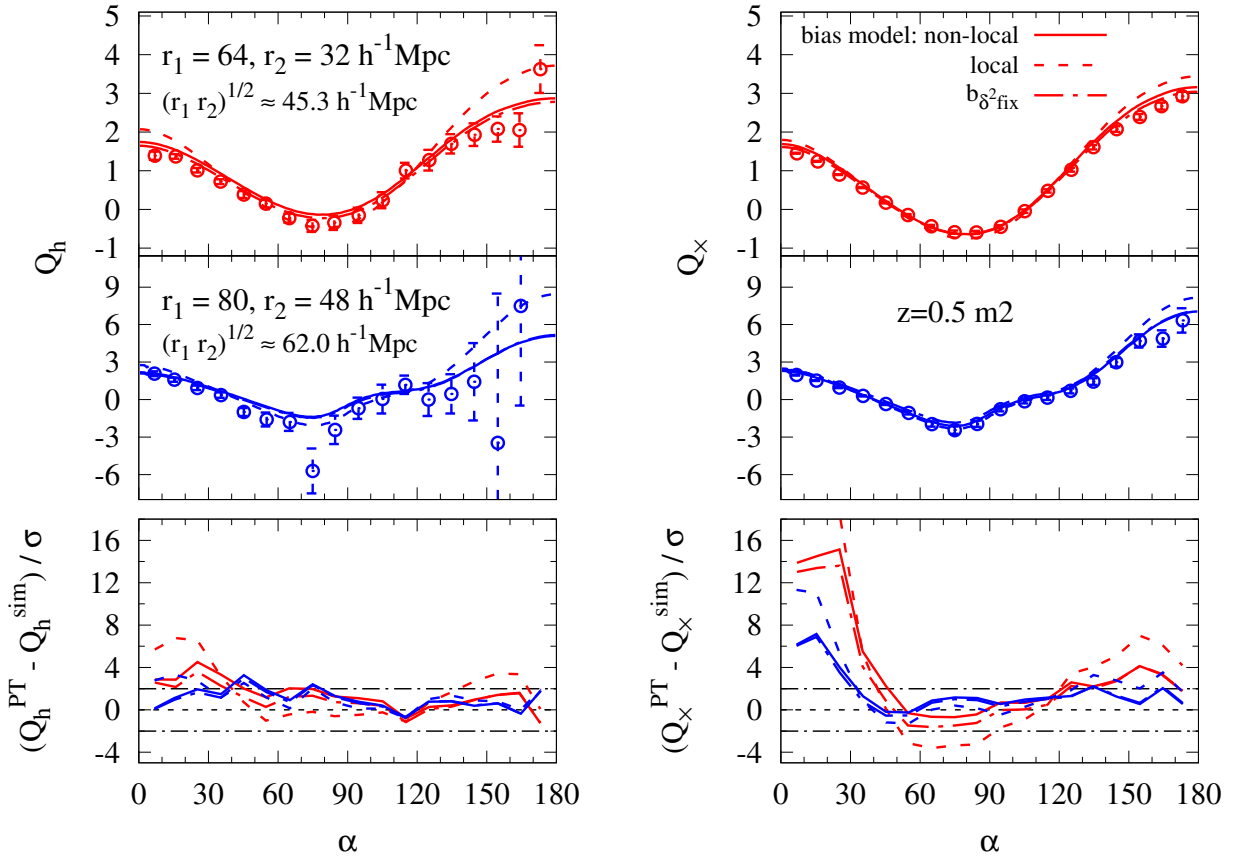


Figure 9. Left: top panels show the reduced halo 3PCF, Q_h , for triangles with fixed legs r_1 and r_2 (size is indicated in $h^{-1}\text{Mpc}$) versus the mean triangle opening angle per bin, $\alpha \equiv \arccos(\hat{\mathbf{r}}_1 \cdot \hat{\mathbf{r}}_2)$. Symbols show mean measurements from 49 simulations with 1σ errors for the mass sample m2 at redshift $z = 0.5$. Lines show predictions from equation (5), using the non-linear power spectrum and the bias models from Table 1 with bias parameters measured by CSS12 in Fourier space. The bottom panel shows the significance of the deviations between model predictions and measurements. Right: analogous results for the reduced three-point halo-matter cross-correlations, while predictions are derived from equation (6).

of the Q_h model beyond leading order might only lead to a marginal improvement of the model performance.

In Fig. 10 we show the comparison between Q_x and Q_h models and measurements for all triangles, displaying them for different scales $\sqrt{r_1 r_2}$ versus the triangle opening angle (as in Fig. 7). Results are shown for the low biased sample m0 at $z = 0.0$ and the highly biased sample m2 at $z = 0.5$. The latter confirm the trends from Fig. 9. In particular for small triangles ($\sqrt{r_1 r_2} \lesssim 40 h^{-1}\text{Mpc}$) the Q_x and Q_h models overpredict the measurements for collapsed and relaxed triangles and underpredict them for triangles with $60 \lesssim \alpha \lesssim 90$. The Q_h results for m2 at $z = 0.5$ are again an exception. In that case the local model is in better agreement with the measurements than the non-local model, which is consistent with the ΔQ results for this sample and might be attributed to a compensation of quadratic non-local and neglected higher-order terms, as mentioned in the discussion of Fig. 6 in Section 3.2. Note that this compensation is shown here to occur for one particular halo sample, while this is not the case for other samples (not shown here).

Overall the results from the non-local bias model are in better agreement with the measurements for the sample m2 at $z = 0.5$ than the local model at large triangle scales

($\sqrt{r_1 r_2} \gtrsim 40 h^{-1}\text{Mpc}$ or $\alpha \gtrsim 90$) and are consistent with those from the $b_{\delta^2\text{fix}}$ model. For the low biased sample m0 at $z = 0.0$ all bias models deliver similar results, since the non-local bias contribution is very weak. For some triangles we find an increased significance of the deviations for that sample, compared to the m2 sample at $z = 0.5$, presumably because the shot noise error contribution is decreased due to the higher halo density. In the case of Q_x , where the shot noise errors are the lowest, the deviations follow the BAO feature, which we saw already in the Q_m model validation (Fig. 7). Using model predictions based on the linear power spectrum, we find a significant increase of the deviations in the case of Q_x for both samples (not shown here). This indicates that neglected terms in the Q_m model, in the bias model or both affect the halo 3PCF, even at very large triangle scales. However, for the auto-correlation Q_h at $\sqrt{r_1 r_2} \gtrsim 40 h^{-1}\text{Mpc}$ their contribution seems to be small compared to the measurement errors, as we find a similarly significant deviations for different power spectra and halo samples. This will in particular be also the case for the smaller volumes, covered by galaxy surveys, for which the measurement errors can be expected to be larger.

The deviations between non-local bias model pre-

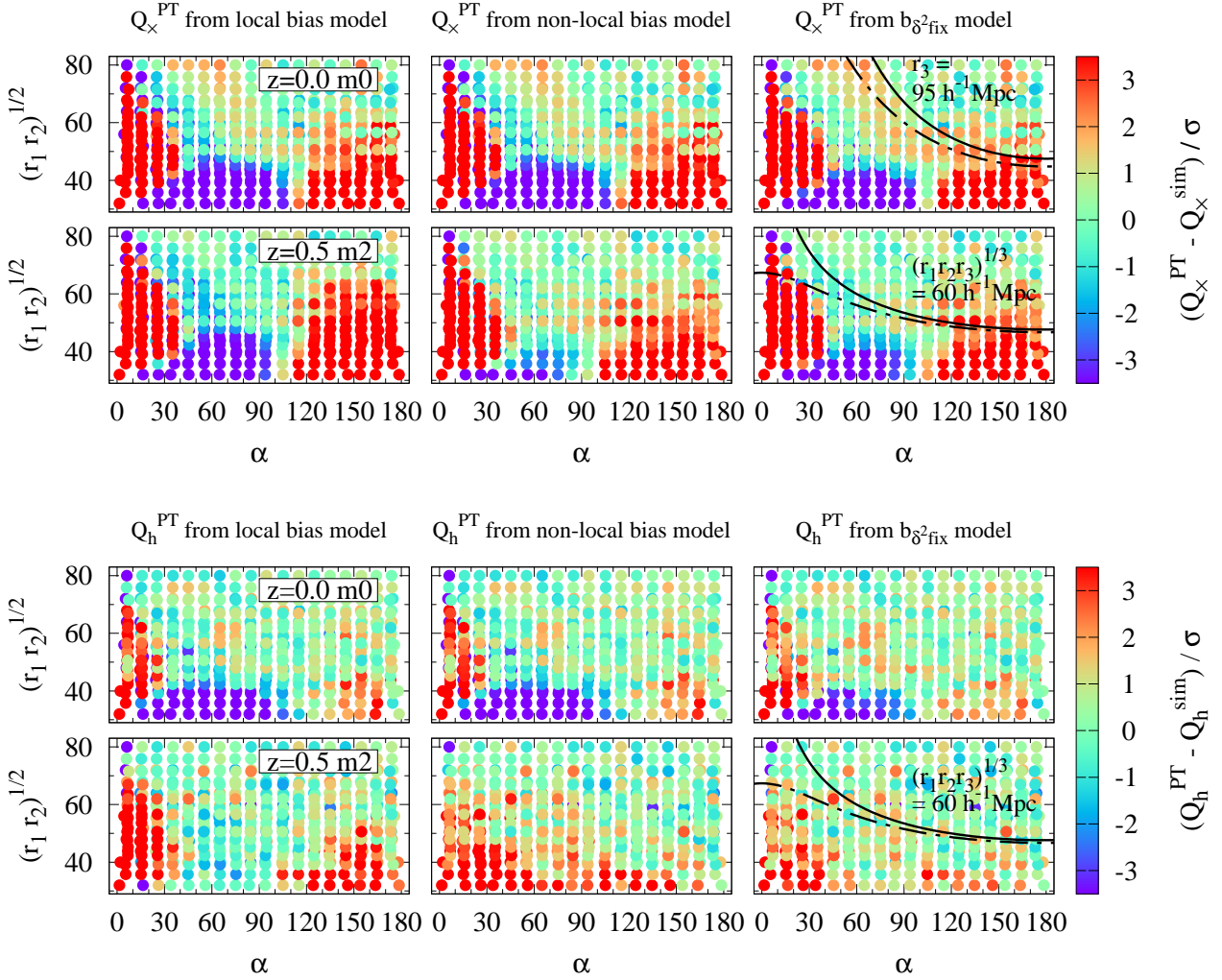


Figure 10. Significance of the deviations between predictions for Q_\times and Q_h and measurements for the mass samples m0 at $z = 0.0$ and m2 at $z = 0.5$ (top, bottom panels respectively). The results are shown versus the mean triangle opening angles per bin, α , and triangle scales $(r_1 r_2)^{1/2}$ in $h^{-1}\text{Mpc}$. The predictions are derived from the bias models described in Table 1, with bias parameters measured in Fourier space by CSS12. Solid and dashed black lines in the bottom right panel show $(r_1 r_2)^{1/2}(\alpha)$ for $(r_1 r_2 r_3)^{1/3} = 60 h^{-1}\text{Mpc}$ and triangle configurations of $r_1/r_2 = 0.5$ and 1.0 respectively.

dictions and measurements converge to values of $\lesssim 2\sigma$ $(r_1 r_2 r_3)^{1/3} \gtrsim 60 h^{-1}\text{Mpc}$ (marked in Fig. 10 as black lines) for both, Q_\times and Q_h , as shown in Fig. A4 and A5. This is consistent with our corresponding results for Q_m and ΔQ .

As in the case of Q_m and ΔQ , measurements of Q_h and Q_\times from different triangles are covariant (see Fig. B1). Quantifying the significance of deviations between model predictions and measurements, we show in Fig. 11 the $\chi^2/d.o.f.$ in bins of $(r_1 r_2 r_3)^{1/3}$ for all three mass samples and redshifts. Each bin contains measurements from 30 triangles and the χ^2 values have been computed via SVD (see Section 2.4) using only the dominant modes, as for the Q_m and ΔQ analyses from Fig. 5 and 8. We also tested that our results are not affected by the chosen number of triangles per bin. The results confirm the convergence of the deviations to $1 - 2\sigma$ for $(r_1 r_2 r_3)^{1/3} \gtrsim 60 h^{-1}\text{Mpc}$. However, they show strong variations for different scales, which might result from noise in our covariance estimation from only 49 realisations. Overall, the $\chi^2/d.o.f.$ values for Q_\times are higher than those for

Q_h , presumably because of the higher signal-to-noise ratio of the measurements. Even at large scales above $60 h^{-1}\text{Mpc}$ we find $\chi^2/d.o.f. \simeq 5$ values. They might be explained by non-linearities around the BAO feature, which are not fully captured in our leading order perturbative model (see Fig. 10). For Q_\times the $\chi^2/d.o.f.$ values are lower at high redshift and higher mass samples. The latter result might be explained by larger shot-noise errors on the high mass samples and agrees with the results from Fig. A4 and A5. Smaller deviations at high redshifts might result from a smaller impact of next to leading order terms in the Q_\times model, which we neglect in our analysis. We do not see a clear dependence of the results on mass and redshift for Q_h , possibly because of the low signal-to noise ratio. It is interesting to note that the $\chi^2/d.o.f.$ values for the $b_{\delta^2 \text{fix}}$ model are in very good agreement with those from the non-local model for highly biased sample (high halo mass and redshift). For samples with low bias (low mass, low redshift) the $\chi^2/d.o.f.$ values for the $b_{\delta^2 \text{fix}}$ are even smaller than those for the non-local

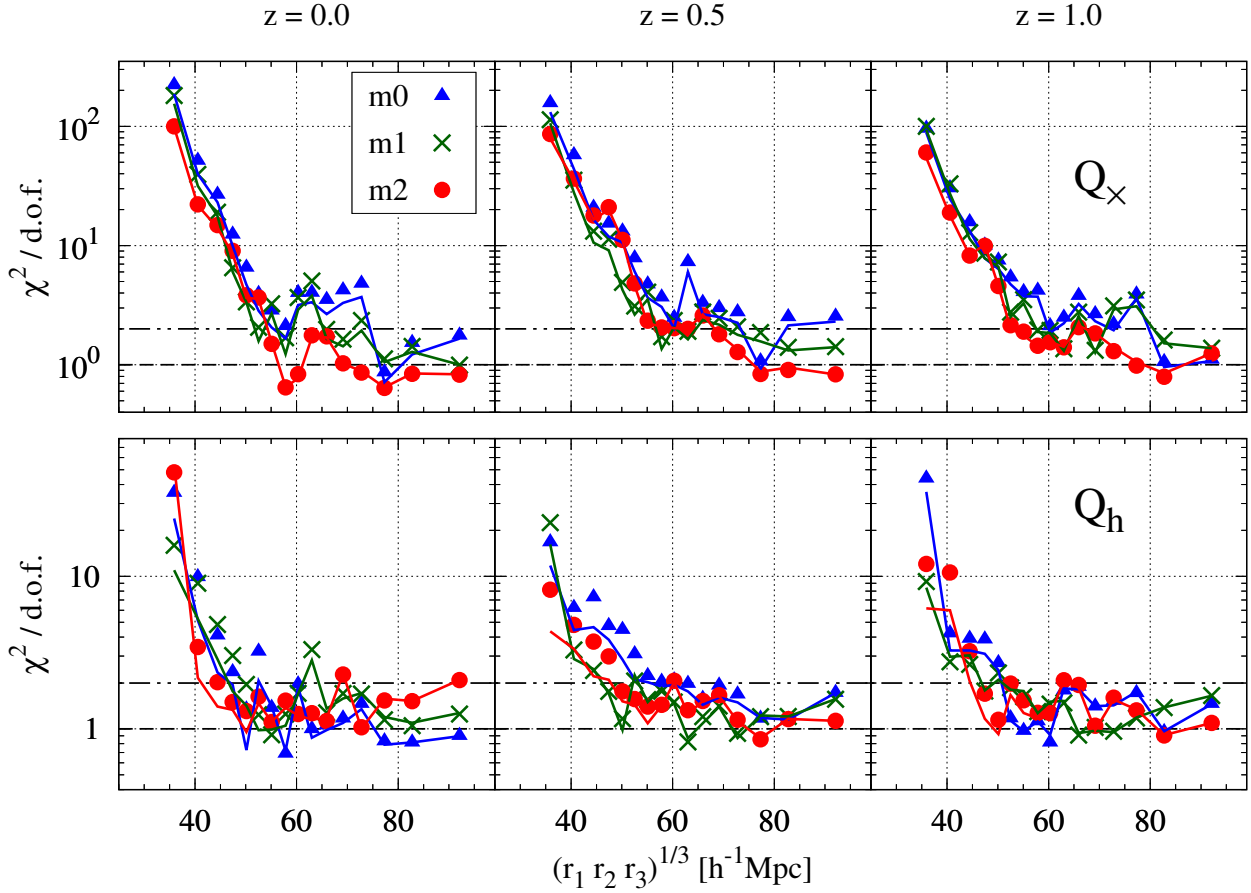


Figure 11. Top: χ^2 per degree of freedom (d.o.f.), quantifying the difference between the Q_\times measurements for the mass samples m1, m2, m3 (defined in Table 2) and the corresponding predictions, based on the non-linear power spectrum at different redshifts z . Symbols show results for the non-local bias model, while lines show results using analytical relations between the linear and non-linear bias parameters ($b_{\delta^2 \text{fix}}$ model, see Table 1). The bias parameters were measured by CSS12 in Fourier space. Bottom: same as top panel, but for Q_h .

model. The latter finding is consistent with our model comparison for ΔQ .

Our comparison between $\chi^2/\text{d.o.f.}$ values for local and non-local model predictions in Fig. 12 demonstrates that setting the non-local term in the prediction to zero leads to higher deviations from Q_\times measurements for highly biased samples. The effect is also apparent for Q_h , even for $(r_1 r_2 r_3)^{1/3} > 60 \text{ h}^{-1} \text{Mpc}$, while in that case the $\chi^2/\text{d.o.f.}$ values are lower, presumably due to larger errors on the measurements. Again these results confirm those for ΔQ , shown in Fig. 8.

4 SUMMARY AND CONCLUSIONS

The main result of this paper (summarized in Fig. 11) is an empirical determination of the scales at which three-point halo correlations in configuration space are consistent with the corresponding statistics in Fourier space, i.e. the bispectrum. To this end, we measured the reduced three-point auto-correlation function of matter and halos, as well as the reduced halo-matter three-point cross-correlation (which are referred to as Q_m , Q_h and Q_\times respectively) in a set of 49 cosmological simulations with a total volume of

$\sim 100 (h^{-1} \text{Gpc})^3$. The large volume provides small errors on the measurements. At the same time we obtain rough estimates of the error covariances, which we analysed using singular value decomposition. The Q_h and Q_\times measurements were compared to leading order perturbative models (equation (5) and (6)), which relate these statistics to Q_m via the linear, quadratic and non-local bias parameters (referred to as b_1 , c_2 and g_2 respectively). For testing the consistency with results from Fourier space, we adopted bias parameters, which were measured in the same set of simulations by Chan et al. (2012, referred to as CSS12) using the same perturbative model of the halo-matter cross-bispectrum.

We adopted the bias parameters in three different ways. The first way is to simply employ the set of Fourier space parameter from CSS12. The second set of parameters are identical to the first set, except for the non-local bias parameter g_2 , which is set to zero in order to study the contribution of the non-local terms to the Q_h and Q_\times predictions. For the third set we used the linear bias, measured by CSS12 from the halo-matter cross-power spectrum, while the quadratic bias is set by the (approximately) universal $c_2(b_1)$ relation from Hoffmann et al. (2017) and the non-local bias is predicted using the $g_2(b_1)$ relation from the local Lagrangian model, reducing the degrees of freedom in the bias

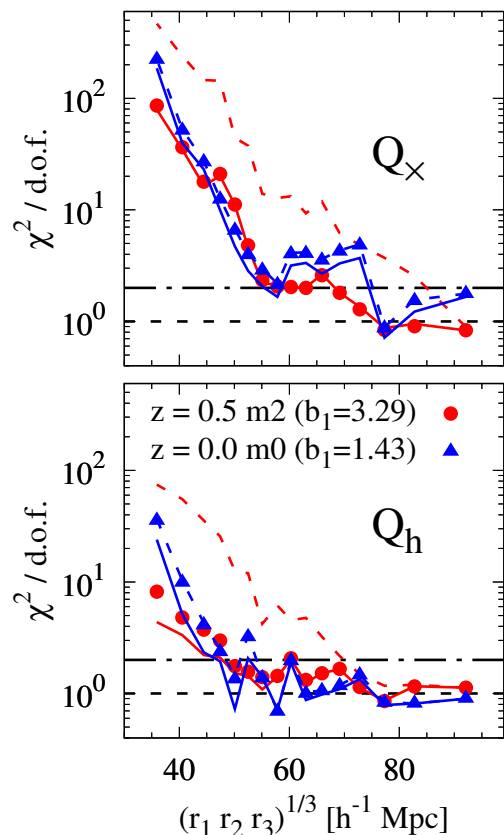


Figure 12. The figure shows the same results for the non-local and b_{δ^2fix} model as shown in Fig. 11 for the mass sample m0 at $z = 0.0$ m2 at $z = 0.5$. In addition we show here results for the local model as dashed lines.

model. These three sets of bias parameters are referred to as non-local, local and b_{δ^2fix} model respectively and are summarized in Table 1.

Before predicting Q_h and Q_\times using the bias parameters, we first had to obtain the matter contribution Q_m and the non-local contribution Q_{nloc} . To remain closer to an analysis of observational data, where these quantities cannot be directly measured, we modeled them from the linear, the linear de-wiggled and the non-linear power spectrum. By comparing the Q_h and Q_\times predictions to measurements, we therefore did not only test if the bias parameters in Fourier space describe the clustering in configurations space, but also simultaneously at which scales the perturbative model of the three-point correlation breaks down. We conducted this comparison in three steps. We first studied in Section 3.1 how well Q_m measurements are described by the leading order perturbative predictions from the different power spectra. Secondly, we investigate how well the higher-order contributions to Q_h are described by the leading (quadratic) order perturbative models, based on the Fourier space bias parameters. These contributions are obtained from the measurements by the subtraction $\Delta Q \equiv Q_h - Q_\times$, as described in Section 3.2. Finally, we compare in Section 3.3 the full predictions for Q_h and Q_\times with the corresponding measurements.

Overall our results show that the deviations between the model predictions for Q_m , Q_h , Q_\times and ΔQ and the corresponding measurements depends on the triangle scale as well as on the triangle shape (characterised by the triangle opening angle) for which these statistics are studied. The quantity $(r_1 r_2 r_3)^{1/3}$ turns out to be a convenient definition of the triangle scale, since it shows a tight correlation with the measurement errors. Furthermore it separates well larger triangles for which the models perform well from smaller ones, for which the measurements are presumably strongly affected by higher order terms. We found that the deviation between the perturbative model predictions of the different three-point correlations from the measurements converge to the $1-2\sigma$ level for $(r_1 r_2 r_3)^{1/3} \gtrsim 60 h^{-1} \text{Mpc}$, while the noisy error estimation imposes some uncertainty on this value. Note here that the smallest r_i value above zero in our analysis corresponds to the size of the $8 h^{-1} \text{Mpc}$ grid cells into which we divided the simulations for computing the correlations. However, when the measurement errors are small (in particular their shot-noise contribution), which is the case for Q_m and Q_\times , and when the predictions are computed from the linear instead of the non-linear power spectrum, we find deviations above 2σ for $(r_1 r_2 r_3)^{1/3} \gtrsim 60 h^{-1} \text{Mpc}$. We attribute this effect to non-linearities around the BAO peak from large scale displacements and bias contributions not included in our treatment. The fact that this effect is much weaker when using the de-wiggled, or the non-linear power spectrum indicates that the latter can incorporate higher orders in the perturbative model for Q to some degree.

Validating the model for the quadratic terms in Q_h and Q_\times with the ΔQ measurements, we found the predictions based on the non-local bias model to show an overall better performance than those from the local model. An exception are measurements in highly biased halo samples from small triangles with intermediate opening angles, which are better described by the local than the non-local bias model. We interpret this effect as a compensation of the non-local and the higher order terms not included in our bias treatment, which occurs for these particular triangles and this particular halo sample.

Interestingly, the deviations of the ΔQ predictions based on the b_{δ^2fix} bias model from the measurements are similar, and for low biased samples even smaller than those based on the non-local model. For $(r_1 r_2 r_3)^{1/3} \gtrsim 60 h^{-1} \text{Mpc}$ the significance of the deviations between ΔQ predictions and measurement is similar for all bias models, presumably because of the low signal-to-noise ratio.

From the Q_\times measurements we conclude that the leading order perturbative model predictions in combination with the bias derived from the same statistics in Fourier space are a good approximation, with $1-2\sigma$ deviations $(r_1 r_2 r_3)^{1/3} \gtrsim 60 h^{-1} \text{Mpc}$. These deviation are slightly higher around the aforementioned BAO feature, but given the small errors on Q_\times this agreement is still good. The model performance for Q_h at large scales is even better, despite the fact that terms beyond leading order, which are neglected in the model should affect Q_h more strongly than Q_\times . This might be a result of the lower signal-to-noise ratio. However, the Q_h predictions differ significantly from the measurements for $(r_1 r_2 r_3)^{1/3} \lesssim 50 h^{-1} \text{Mpc}$. It is thereby important to note, that these results are specific to our small measurement errors from the combined $\sim 100 (h^{-1} \text{Gpc})^3$ of the

49 simulations studied in this work. In practice, the deviation between model predictions and measurements can be expected to be less significant, as the measurement errors are larger for the smaller volumes of current and upcoming galaxy surveys.

As for ΔQ , the Q_h and Q_\times predictions from the $b_{\delta^2 fix}$ model agree equally well with the measurements at large scales for highly biased samples (high masses, high redshift). For low biased samples (low mass, low redshift) this model describes the Q_h and Q_\times measurements even better than the non-local model. Differences in the Q_h predictions based on the linear and non-linear power spectrum are negligible compared to the larger measurement errors.

The good performance of predictions from the $b_{\delta^2 fix}$ model at large scales suggests that a roughly universal $c_2(b_1)$ relation, together with the local Lagrangian $g_2(b_1)$ relation, could tighten constraints on the linear bias, derived from third-order statistics in galaxy surveys. However, recent studies pointed out, that assembly bias can lead to deviations from a universal $c_2(b_1)$ relation (Modi et al. 2016; Paranjape & Padmanabhan 2017). An application of the $b_{\delta^2 fix}$ model in the analysis of galaxy surveys therefore requires tests in mock catalogues (for instance from semi-analytic models of galaxy formation) to validate for which type of galaxy samples these bias relations are useful approximations. More generally, the results presented in this paper show a good overall agreement of the non-local quadratic bias models with simulations, using the same bias parameters for Fourier and configuration space, but the range of validity will depend strongly on the samples used (volume, redshift and bias), so a detailed comparison with mock galaxy and corresponding dark matter catalogues with redshift space distortions will be needed.

ACKNOWLEDGEMENTS

We acknowledge support from the Spanish Ministerio de Ciencia e Innovación (MICINN) projects AYA2012-39559 and AYA2015-71825, and research project 2014 SGR 1378 from the Generalitat de Catalunya. KH acknowledges the support by the International postdoc fellowship from the Chinese Ministry of Education and the State Administration of Foreign Experts Affairs. He also thanks the organisers and participants of the workshop *Biased Tracers of Large-Scale Structure* at the Lorentz Center as well as Kwan Chuen Chan for useful discussions. MC acknowledges support from the MICINN project AYA2013-44327 and the Ramon y Cajal program.

References

Baldauf T., Seljak U., Desjacques V., McDonald P., 2012, *Phys. Rev. D*, **86**, 083540
 Baldauf T., Mirbabayi M., Simonović M., Zaldarriaga M., 2015, *Phys. Rev. D*, **92**, 043514
 Barriga J., Gaztañaga E., 2002, *MNRAS*, **333**, 443
 Bel J., Hoffmann K., Gaztañaga E., 2015, *MNRAS*, **453**, 259
 Berlind A. A., Weinberg D. H., 2002, *ApJ*, **575**, 587
 Blas D., Garny M., Ivanov M. M., Sibiryakov S., 2016, *J. Cosmology Astropart. Phys.*, **7**, 028
 Carlson J., Reid B., White M., 2013, *MNRAS*, **429**, 1674

Chan K. C., Blot L., 2016, preprint, ([arXiv:1610.06585](#))
 Chan K. C., Scoccimarro R., Sheth R. K., 2012, *Phys. Rev. D*, **85**, 083509
 Cooray A., Sheth R., 2002, *Phys. Rep.*, **372**, 1
 Crocce M., Scoccimarro R., 2008, *Phys. Rev. D*, **77**, 023533
 Desjacques V., Jeong D., Schmidt F., 2016, preprint, ([arXiv:1611.09787](#))
 Eisenstein D. J., Hu W., 1998, *ApJ*, **496**, 605
 Eisenstein D. J., Seo H.-J., White M., 2007, *ApJ*, **664**, 660
 Frieman J. A., Gaztanaga E., 1994, *ApJ*, **425**, 392
 Fry J. N., 1984, *ApJ*, **279**, 499
 Fry J. N., Gaztanaga E., 1993, *ApJ*, **413**, 447
 Gaztañaga E., Scoccimarro R., 2005, *MNRAS*, **361**, 824
 Gaztañaga E., Cabré A., Castander F., Crocce M., Fosalba P., 2009, *MNRAS*, **399**, 801
 Gaztanaga E., Bernardeau F., 1998, *A&A*, **331**, 829
 Gil-Marín H., Noreña J., Verde L., Percival W. J., Wagner C., Manera M., Schneider D. P., 2015, *MNRAS*, **451**, 539
 Hartlap J., Simon P., Schneider P., 2007, *A&A*, **464**, 399
 Hoffmann K., Bel J., Gaztañaga E., Crocce M., Fosalba P., Castander F. J., 2015a, *MNRAS*, **447**, 1724
 Hoffmann K., Bel J., Gaztañaga E., 2015b, *MNRAS*, **450**, 1674
 Hoffmann K., Bel J., Gaztañaga E., 2017, *MNRAS*, **465**, 2225
 Jarvis M., 2015, TreeCorr: Two-point correlation functions, Astrophysics Source Code Library (ascl:1508.007)
 Jing Y. P., Boerner G., 1997, *A&A*, **318**, 667
 Lazeyras T., Wagner C., Baldauf T., Schmidt F., 2016, *J. Cosmology Astropart. Phys.*, **2**, 018
 Li C., Jing Y. P., Kauffmann G., Börner G., Kang X., Wang L., 2007, *MNRAS*, **376**, 984
 Manera M., Gaztañaga E., 2011, *MNRAS*, **415**, 383
 Marín F. A., et al., 2013, *MNRAS*, **432**, 2654
 McBride C. K., Connolly A. J., Gardner J. P., Scranton R., Newman J. A., Scoccimarro R., Zehavi I., Schneider D. P., 2011a, *ApJ*, **726**, 13
 McBride C. K., Connolly A. J., Gardner J. P., Scranton R., Scoccimarro R., Berlind A. A., Marín F., Schneider D. P., 2011b, *ApJ*, **739**, 85
 McDonald P., Roy A., 2009, *J. Cosmology Astropart. Phys.*, **8**, 020
 Modi C., Castorina E., Seljak U., 2016, preprint, ([arXiv:1612.01621](#))
 Müller V., Hoffmann K., Nuza S. E., 2011, *Baltic Astronomy*, **20**, 259
 Paranjape A., Padmanabhan N., 2017, *MNRAS*, **468**, 2984
 Peebles P. J. E., Groth E. J., 1975, *ApJ*, **196**, 1
 Pollack J. E., Smith R. E., Porciani C., 2012, *MNRAS*, **420**, 3469
 Pujol A., et al., 2017, *MNRAS*, **469**, 749
 Scoccimarro R., 2000, *ApJ*, **544**, 597
 Scoccimarro R., Colombi S., Fry J. N., Frieman J. A., Hivon E., Melott A., 1998, *ApJ*, **496**, 586
 Scoccimarro R., Sheth R. K., Hui L., Jain B., 2001, *ApJ*, **546**, 20
 Sefusatti E., Crocce M., Pueblas S., Scoccimarro R., 2006, *Phys. Rev. D*, **74**, 023522
 Sefusatti E., Crocce M., Desjacques V., 2010, *MNRAS*, **406**, 1014
 Senatore L., Zaldarriaga M., 2015, *J. Cosmology Astropart. Phys.*, **2**, 013
 Slepian Z., Eisenstein D. J., 2015, *MNRAS*, **454**, 4142
 Slepian Z., et al., 2017, *MNRAS*, **469**, 1738
 Springel V., et al., 2017, preprint, ([arXiv:1707.03397](#))
 Srednicki M., 1993, *ApJ*, **416**, L1

APPENDIX A: DEVIATIONS FOR INDIVIDUAL TRIANGLES

The errors of the different Q measurements correlates strongly with the total triangle scale, defined by $(r_1 r_2 r_3)^{1/3}$

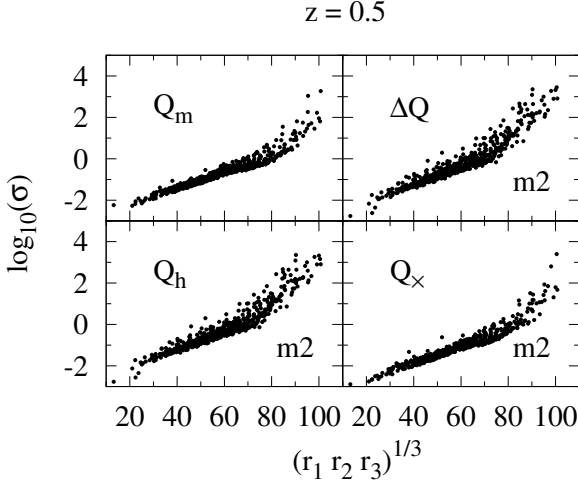


Figure A1. Examples of 1σ errors of the different reduced 3PCFs studied in this paper versus the triangle scale. Results for different redshifts and mass samples are similar.

as shown in Fig. A1. We therefore study here the significance of the deviations between measurements and predictions versus this scale.

Fig. A2 shows that the Q_m predictions deviate from the measurements by less than 2σ for $(r_1 r_2 r_3)^{1/3} \gtrsim 80$ when predictions are computed from the linear power spectrum and $\gtrsim 60 h^{-1}\text{Mpc}$ when using the non-linear power spectrum. Note that these results are specific for the joint $\sim 100 (\text{Gpc}/h)^3$ volume of the 49 simulations. For smaller volumes (as covered by current galaxy surveys) errors would be larger and the significance therefore smaller. Using alternative measures for the triangle scale, such as the triangle area or the sum of the triangle legs leads to a less clear separation between triangles with weak and strong significance of the deviations.

The corresponding results for ΔQ are shown in Fig. A3 for the low biased sample (m0) at $z = 0.0$ and the highly biased sample (m2) at $z = 0.5$ (with $b_1 = 1.43$ and $b_1 = 3.29$ respectively). For the sample with the low linear bias the model predictions are below the measurements at $(r_1 r_2 r_3)^{1/3} \lesssim 60 h^{-1}\text{Mpc}$. Differences between local and non-local model predictions are not apparent, as expected from Fig. 7. For the sample with the higher linear bias the predictions are above the measurements for $(r_1 r_2 r_3)^{1/3} \gtrsim 60 h^{-1}\text{Mpc}$ and the non-local model performs slightly better than the local model at small scales. At large scales differences between model and predictions are not significant for both samples, due to the low signal-to-noise ratio, which is shown in the bottom panel of Fig. A3. Note that the predictions are based on the non-linear power spectrum, measured in the simulation, while the linear power spectrum leads to very similar results.

The significance of the deviations between non-local bias model predictions for Q_h and Q_x and the corresponding measurements are displayed versus the triangle scale in Fig. A4 and A5. Covering a larger range of bias values ($1.43 \lesssim b_1 \lesssim 3.99$), we now show results for the mass samples m0 and m2, each at redshift $z = 0.0$ and 1.0 . Also here the predictions are based on the non-linear power spectrum and we find very similar results when using the linear

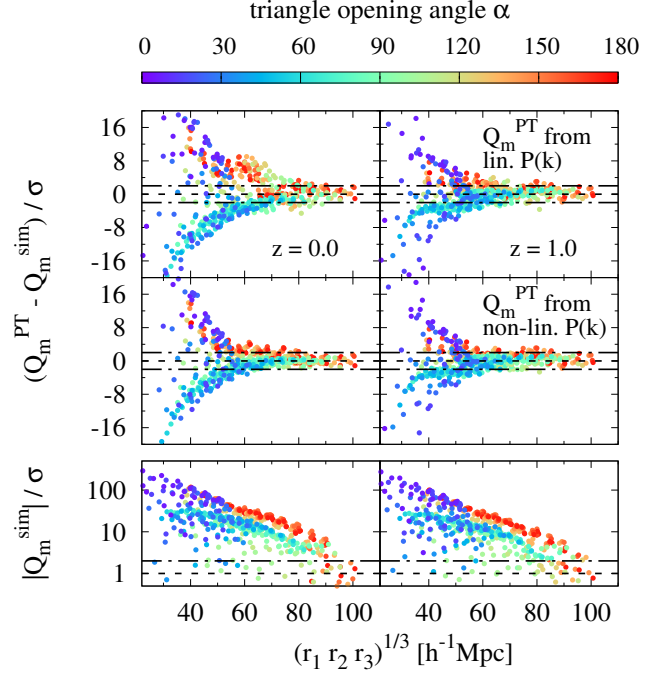


Figure A2. Top panels: Significance of the deviation between Q_m measurements and tree-level predictions (based on the linear and non-linear power spectrum) versus the triangle scale. Dashed-dotted lines denote 2σ deviations. Bottom panel: Signal-to-noise ratio. Colours denote the triangle opening angle.

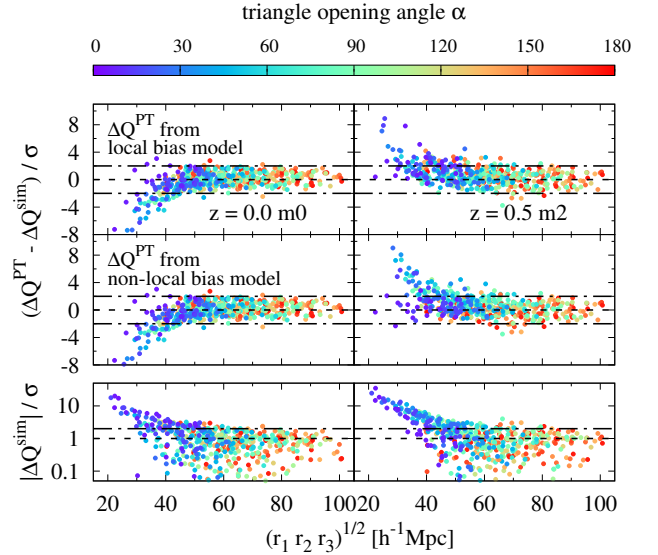


Figure A3. Significance of the deviation between predictions for ΔQ and measurements versus triangle scale $(r_1 r_2 r_3)^{1/3}$ for the halo mass samples m0 at $z = 0.0$ and m1 at $z = 0.5$ (left and right panels respectively). The top and central panels show results for predictions from the local and non-local model respectively (Table 1), based on the non-linear power spectrum. The bottom panel shows signal-to-noise ratio of measurements.

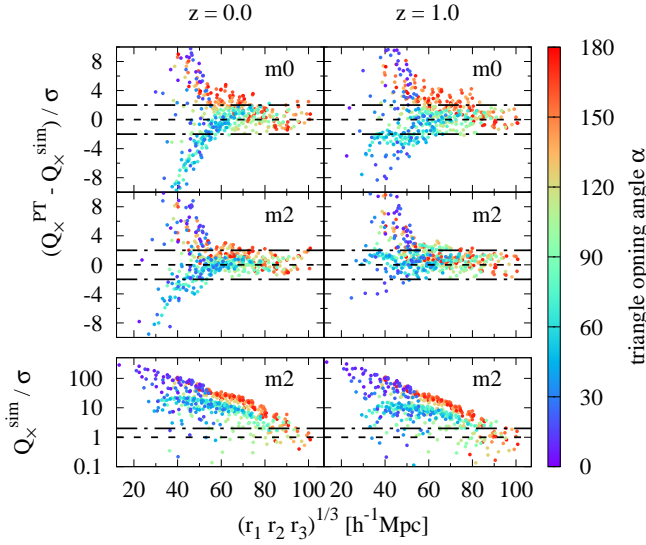


Figure A4. Significance of the deviations between predictions for Q_\times and measurements versus triangle scale $(r_1 r_2 r_3)^{1/3}$. The predictions are based on the non-local bias model (Table 1) and the non-linear power spectrum. Results are shown for the halo mass samples m0 and m2 at $z = 0.0$ and $z = 1.0$ (left and right, top, bottom panels respectively). The lower sub panels show the signal-to-noise ratios for the samples m2, which have higher shot-noise contributions than the m0 sample.

power spectrum. The results are consistent with those shown in Fig. 10 as the predictions are most significant for small triangles, where they show a strong dependence on the triangle opening angle for low biased samples, while samples with high bias (higher masses and redshifts) show a weaker dependence on the opening angle at small scales. Overall the deviations for both, Q_\times and Q_h converge to values of $\lesssim 2\sigma$ for all samples for $(r_1 r_2 r_3)^{1/3} \gtrsim 60 h^{-1} \text{Mpc}$. An exception are results Q_\times for large opening angles, which can be attributed non-linearities around the BAO peak, as mentioned in the discussion of Fig. 10.

APPENDIX B: COVARIANCES

In Fig. B1 we show examples of the normalised covariance matrices at $z = 0.5$ for the different three-point statistics versus the triangle scale $(r_1 r_2 r_3)^{1/3}$. The covariances for Q_m and Q_\times show strong off-diagonal elements, while those of Q_h and ΔQ are dominated by the diagonal elements, which indicates high shot-noise contributions. Subsets of these covariances with 30^2 elements around the diagonal are used for the χ^2 estimation, described in Section 2.4.

In order to reduce the impact of noise on these estimations we perform a singular value decomposition of the covariances. The distribution of singular values is shown in Fig. B2 and reveals that a significant fraction of modes has only a minor contribution to the covariance. One can see how the singular values for the shot-noise dominated covariances of ΔQ and Q_h show a slightly more pronounced drop, while those of the Q_m and Q_\times covariances decay more slowly. We associate modes below $\lambda^2 \lesssim \sqrt{2/N_{\text{sim}}}$ with noise

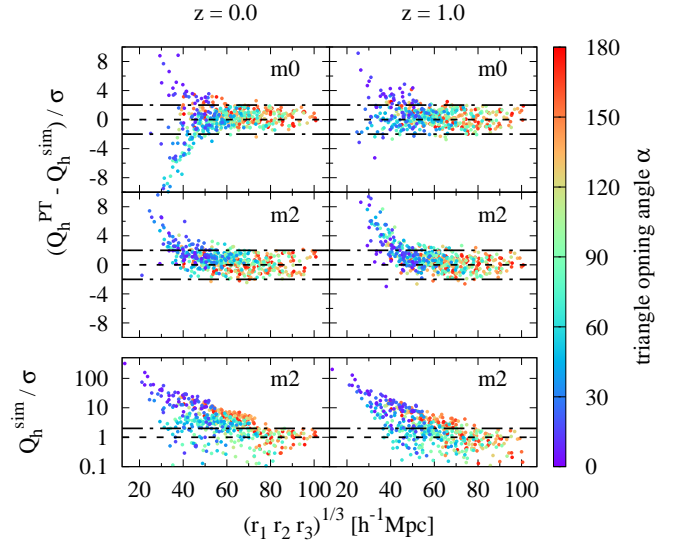


Figure A5. same as Fig. A4, but for Q_h .

in the covariance measurement and neglect them in the χ^2 computation.

This paper has been typeset from a \LaTeX file prepared by the author.

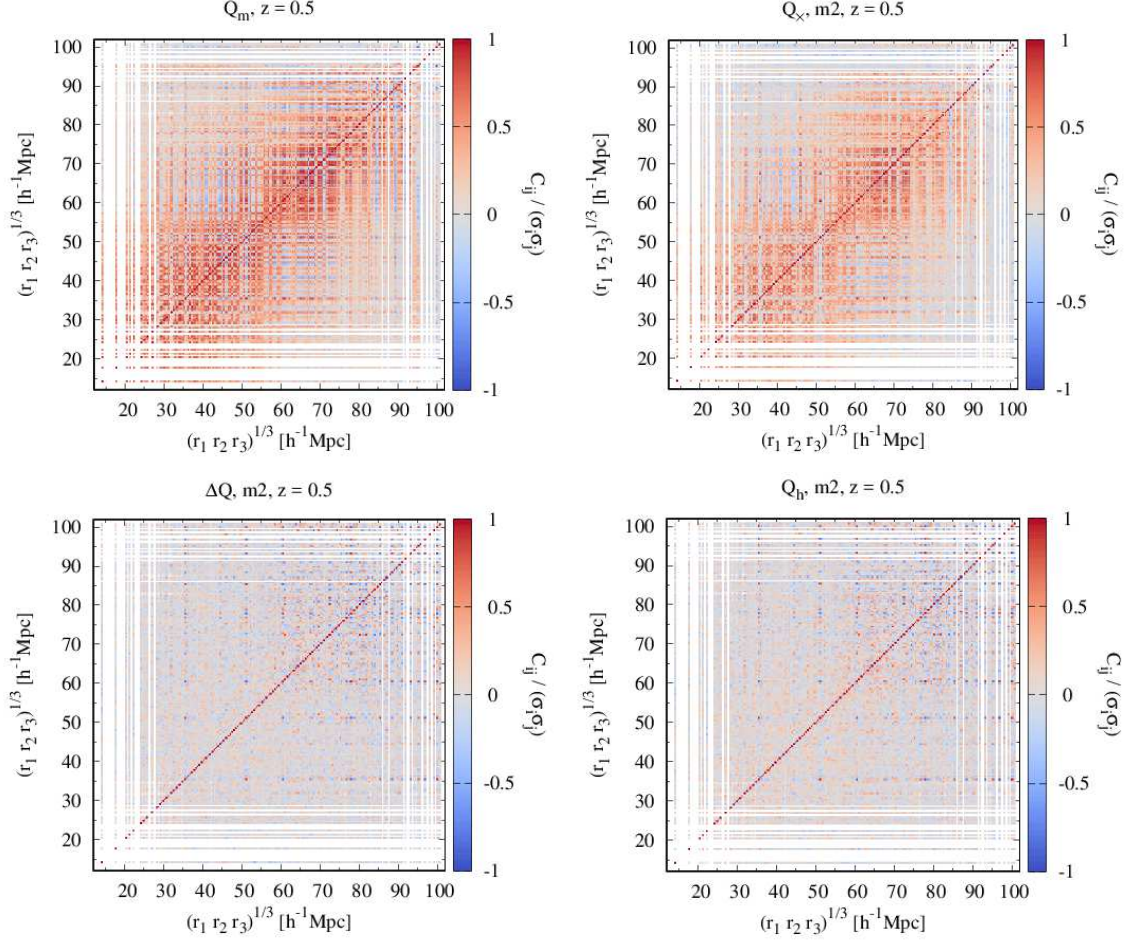


Figure B1. Examples of normalised covariances between different reduced 3PCS from the 504 triangles used in this work. They were obtained from a set of 49 simulations. The low amplitude of the off-diagonal elements in the Q_h covariances indicates a dominance of shot-noise errors. Results for Q_h and Q_x are almost identical, because the Q_x errors are dominated by the Q_h contribution. For computing the χ^2 deviation from the model prediction we select triangles in scale bins containing 30 triangles and perform a singular value decomposition, as described in Section 2.3.

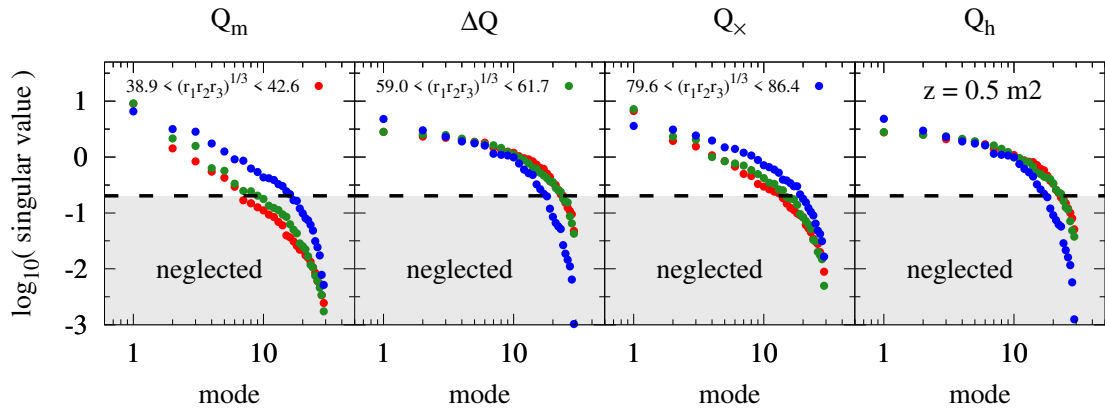


Figure B2. Singular values of the covariance matrices for the different three-point statistics studied in this work versus the mode number. The maximum mode number corresponds to the number of triangles in the $(r_1 r_2 r_3)^{1/3}$ bins. Results are shown for the mass sample m1 at $z = 0.5$. Modes with singular values of less than $\lambda^2 \lesssim \sqrt{2/N_{sim}}$ are associated with noise and therefore neglected in the χ^2 computation. The total number of modes is 30, which corresponds to the number of triangles in each $(r_1 r_2 r_3)^{1/3}$ bin.